Brodogradnja Volume 76 Number 2 (2025) 76203

journal homepage: www.brodogradnja.fsb.hr

Brodogradnja

An International Journal of Naval Architecture and Ocean Engineering for Research and Development

Effect of panel method codes in estimating the time-domain responses of floating wind turbines

Muhammed Ucar[1,2], *Mohamad Hmedi*[3], *Emre Uzunoglu*[4,5], *Elif Oguz*[1,6*]

[1]*Hydraulics Laboratory, Civil Engineering Department, Middle East Technical University, 06800, Ankara, Türkiye*
[2]*Civil Engineering Department, Necmettin Erbakan University, 42140, Konya, Türkiye*
[3]*Alcatel Submarine Networks Marine, 92150, Suresnes, France*
[4]*Centre for Marine Technology and Ocean Engineering (CENTEC), Instituto Superior Técnico, Universidade de Lisboa, 1049-001, Lisbon, Portugal*
[5]*KONGSTEIN AS, 5257, Bergen, Norway*
[6]*METU Center for Wind Energy Research (ODTÜ RÜZGEM), 06800, Ankara, Türkiye*

ARTICLE INFO

Keywords:
Floating wind turbines
Panel method
Hydrodynamics
Time domain analysis
Frequency domain analysis
Boundary element method
Potential flow solver

ABSTRACT

This study investigates the impact of frequency-domain hydrodynamic outputs from several panel method codes on estimating time domain responses of floating wind turbines. The tools under examination are WAMIT and three open-source codes (HAMS, NEMOH, and BEMUse). The panel method codes deliver hydrodynamic coefficients and exciting forces in the frequency domain. The results serve as inputs to time-domain simulations, from which the coupled responses are calculated. Hence, the differences in frequency-domain inputs are reflected in the time-domain. Two platforms are employed: OC3-Hywind spar and OC4-DeepCWind semi-submersible. Discrepancies between hydrodynamic coefficients, excitation forces, and response amplitude operators are inspected. Then, the floaters' time-domain responses are questioned in operational and extreme environmental conditions. The findings highlight limited reflection of frequency-domain differences on the platform motions in time-domain.

1. Introduction

Most offshore wind resources are found in waters exceeding sixty meters in depth [1] and require floating platforms rather than fixed foundations. These platforms must be optimized for site-specific environmental conditions that affect the motion responses of floating wind turbines (FWTs). Floater optimization studies require a high number of simulations [2] with associated computational costs [3]. Therefore, high-fidelity time-domain approaches are impractical during initial design phases [4]. Instead, commonly employed methods involve frequency domain analyses using Morison's equation or potential flow solvers (PFSs). Since the diameter/wavelength ratios of the members in the current floaters exceed 0.2 [5], PFSs are eligible for such platforms. The solvers deliver the excitation forces and the hydrodynamic coefficients in frequency domain (FD). Time-domain simulators then use the FD outputs to emulate the responses of the FWTs.

* Corresponding author.
E-mail address: elifoguz@metu.edu.tr

http://dx.doi.org/10.21278/brod76203

Received 01 December 2024; Received in revised form 01 February 2025; Accepted 12 February 2025;
Available online 13 February 2025
ISSN 0007-215X; eISSN 1845-5859

PFSs using the boundary element method (BEM) for fluid flow problems are called panel method codes. The codes under examination were WAMIT, NEMOH, HAMS, and BEMUse. WAMIT is widely used by marine industries [6-8], and has been validated through numerous studies [9-11]. On the other hand, NEMOH [12, 13], HAMS [14, 15], and BEMUse [16] are open-source alternatives with limited validation studies for FWTs [17-19].

The results of open-source options in FD have been compared in numerous studies for wave energy converters (WECs) [20-22]. For instance, Raghavan et al. [22] compared WAMIT, NEMOH, and HAMS for semi-submerged WECs, concluding that HAMS results are closer to WAMIT than NEMOH for hydrodynamic coefficients and response amplitude operators, and HAMS demonstrated significant computational efficiency, compared to NEMOH.

For FWTs, validation studies in FD are mainly limited to the studies of the developers of the open-source alternatives. For BEMUse, Saverin et al. [16] validated the FD outputs of BEMUse, hydrodynamic coefficients, and excitation forces, with those of WAMIT for the OC4-DeepCWind semi-submersible platform. For HAMS [17], CENTEC-TLP is used to compare the results of HAMS and WAMIT. For NEMOH, Kurnia et al. [13] compared NEMOH with HYDOSTAR for a hemisphere and the OC5-DeepCwind semisubmersible. For Capytaine [23] (a Python-based distribution of NEMOH 2.0), Ancellin et al. [19] compared a floating cylinder with a thin heave plate and the OC4-DeepCWind floating wind turbine platform with the results of HAMS and WAMIT. For NEMOH (v3.0), Kurnia and Ducrozet [24] used a truncated cylinder, a truncated cylinder with a thin heave plate, SOFTWIND spar, and OC4-DeepCWind to compare the results with WAMIT, DIODORE and HYDROSTAR. The validation studies reported high agreements except for Capytaine (based on NEMOH v2.0) for cases handling thin heave plates.

Such studies underline the importance of evaluating the reliability of open-source solvers in the context of FWTs, where their performance may vary due to unique structural and environmental interactions. However, it remains unclear whether the differences observed in FD outputs are reflected in the time-domain motion responses of FWTs.

This study investigates the reflections of discrepancies in panel method code outputs on estimating the time-domain responses of FWTs. The secondary purpose of the research is to provide insights into the current state of the open-source codes. The study does not aim to identify the optimal solver; it rather highlights the capabilities of the various tools and discerns the differences in their results.

This paper is organized as follows: First, potential flow theory and relevant solvers are introduced. Next, the selected structures, simulation specifications, and environmental conditions are presented. Then, the sensitivity of the panel method codes to mesh refinement is examined. Subsequently, discrepancies in the frequency-domain results of panel method codes are discussed. Finally, the reflections of these differences in the time domain are analyzed.

2. Theoretical background

This section overviews the theoretical basis, employed codes, and evaluation metrics. Potential flow theory is introduced first, and panel method codes are compared. Next, it is explained how the coupled dynamics code, NREL's FAST, simulates FWTs in the time domain by utilizing the panel method code outputs. Lastly, the metrics used to evaluate the outputs were introduced.

2.1 Potential flow solution and applications

2.1.1 Solution bases

Potential flow theory assumes the fluid ideal, i.e., incompressible and inviscid. Ideal fluid assumption provides computational cost advantages and is applicable in the preliminary design phases of floating platforms. Viscous effects can be neglected for structures with slow motions and without specialized damping devices, as the thin boundary layer causes significantly smaller viscous forces than inertial forces. However, for structures equipped with damping devices, such as heave plates, viscous damping can become significant and must be carefully evaluated.

The base of the potential flow theory is the potential function ϕ, whose gradient (∇) yields the velocity field $\nabla\phi = \vec{V}$. Potential flows are irrotational, defined as $\nabla \times \vec{V} = 0$. Therefore, ϕ satisfies the Laplace equation $\nabla^2\phi = 0$. To solve the Laplace equation, boundary conditions (BC) are defined for three locations. These BCs are no-penetration BC on the floating body,

$$\frac{\partial\phi}{\partial n} - \vec{V}.\vec{n} = 0 \tag{1}$$

seabed BC with no-penetration,

$$\frac{\partial\phi}{\partial z} = 0, \qquad for\ z = -H \tag{2}$$

and linearized free surface BC,

$$\frac{\partial\phi}{\partial z} - \frac{\omega^2\phi}{g} = 0, \qquad for\ z = 0 \tag{3}$$

Laplace equation and the corresponding boundary conditions are all linear, therefore the superposition method can be employed to solve the potential function. Submerged bodies are discretized into surface elements (panels) to solve the BCs. The problem is then transformed into algebraic equations using boundary integral equations for diffraction (ϕ_D) and radiation (ϕ_R) problems $\phi = \phi_D + \phi_R$. The velocity potential is calculated in the form of $\phi = \phi_0(z)\sin(\theta - \omega t)$, resulting in periodic forces. Therefore, potential flow solvers cannot solve time-dependent problems with random wave patterns. For such problems, time-domain simulators use inverse Fourier transformations to generate random waves and combine the outputs from PFSs.

2.1.2 Applications

PFSs using the boundary element method for fluid flow problems are called panel method codes. Panel method codes discretize the wet surfaces of the structures into panels on which dipoles, sources, and vortices are distributed. Then, the strengths of vortices, sources, and dipoles are determined using the free surface Green function. BEM solves linear partial differential equations formulated in the boundary integral form. Alternative approaches to BEM are the finite element method (FEM) [25], finite volume method (FVM) [26-28], or finite difference method (FDM) [29]. Compared to alternative methods, BEM is advantageous computationally as it avoids discretizing the entire fluid domain.

The solvers employed are WAMIT and three open-source codes: HAMS, NEMOH, and BEMUse. Only WAMIT has an extensive user manual [30] and a high-order panel option. On the other hand, open-source codes offer more flexibility by allowing source code modifications, which ease, for instance, code coupling. All codes offer DOS commands as a user interface. Additionally, NEMOH provides MATLAB wrapper files, and BEMUse provides a minimal graphical user interface (GUI). To improve computational efficiency, PFSs offer symmetry options that exploit the structural symmetry axes, reducing the solution domain by mirroring results accordingly.

Compared panel method codes solve the same boundary integral equations [31] using different approaches to solve the free-surface Green functions. The methods used by WAMIT and BEMUse are Newman's [32, 33] and Gauss-Legendre's [16], respectively. A family of series expansions and asymptotic expansions are used in the method used by HAMS [34, 35]. NEMOH uses look-up tables for interpolation [12, 33], which may lead to inaccuracies in overlapping panels [36]. NEMOH also differs from the others due to a lack of parallel processing capability. Table 1 summarizes the features and the versions of the codes. Although HAMS does not specify a release number, the version is dated 8 September 2023. No significant changes have been reported then in HAMS's reference repository [37].

Table 1 Property comparison of WAMIT, NEMOH, HAMS, and BEMUse

Properties	WAMIT	NEMOH	HAMS	BEMUse
Used version	6.414	3.0.0	8 September 2023	1.0.1
Solving potential flow	Yes	Yes	Yes	Yes
Frequency-domain solution	Yes	Yes	Yes	Yes
Time-domain solution	No	No	No	No
Operating system support	Windows and Linux	Windows and Linux	Windows, Linux, and macOS	Windows and Linux
User manual	Extensive	Yes	Yes	No
Being open-source	No	Yes	Yes	Yes
Own meshing tool	No	Yes	No	Yes
Approximation for free-surface Green function	Newman's method	Interpolation from look-up tables	Analytical expansion methods	Gauss-Legendre's method
Symmetry axes	2	1	1	No
Allowing multi-bodies	Yes	Yes	Yes for HAMS-MREL version [38]	No
Handling incomplete panels	Yes	Yes	Yes	Yes
Higher-order panels	Yes	No	No	No
Zero and infinite frequencies	Yes	No	Yes	Yes
Impulse functions	Yes	Yes	No	Yes
Response amplitude operators	Yes	Yes	Yes	Yes
Irregular frequency removal	Yes	Yes	Yes	Yes
Quadratic transfer functions	Yes	Yes	No	No
Generalized modes	Yes	Yes	No	No
Multicore option	Yes (v7.0 and later)	No (Needs source code modifications)	Yes	Yes
Interface	DOS commands	DOS commands (wrapped up in MATLAB)	DOS commands	DOS commands and a minimal GUI

2.2 Solution of floater motions in the time domain

The analysis employs FAST V8.16 [39, 40], a time-domain simulator integrating linear models of aerodynamics, hydrodynamics, structural dynamics, foundation dynamics, controller dynamics, and ice impacts. FAST's hydrodynamic calculations show how the hydrodynamic coefficients and excitation forces are processed from frequency to time domain.

The total external load on the support platform, excluding the loads transmitted from the wind turbine and floater weight, is divided into two parts. The first part is the impulsive hydrodynamic added-mass component represented by $A_{jk}(\infty)$, which is added to the platform mass, M_{jk}. The second part is for hydrodynamic and mooring loads. The total external load acting on the floater, $F_j^{Floater}$, is written as:

$$F_j^{Floater} = -A_{jk}(\infty)\ddot{x}_k + F_j^{Hydro} + F_j^{Lines} \tag{4}$$

where x_k represents the platform displacement, and with dots indicating time derivatives. F_j^{Lines} denotes the mooring line loads, while F_j^{Hydro} includes all hydrodynamic effects except the impulsive added mass

component, $A_{jk}(\infty)$. The subscripts j and k correspond to the floater's six degrees of freedom (DOF) (1 = surge, 2 = sway, 3 = heave, 4 = roll, 5 = pitch, 6 = yaw). Although $A_{jk}(\infty)$ is a hydrodynamic effect, it is grouped with the platform's inertial forces in equation (4) to ensure explicit equations of motion in the time-domain framework of OpenFAST. Following Jonkman's formulation [39], this separation provides numerical clarity by distinguishing between inertial forces (added mass) and other hydrodynamic effects, such as radiation damping and wave excitation.

FAST's HydroDyn module [41] computes loads on the floater by integrating dynamic pressure over its wetted surface. These loads include contributions from incident wave scattering (diffraction), inertia (added mass), linear drag (radiation), sea currents, and nonlinear processes. Additionally, hydrostatic restoring forces, arising from the floater's displaced volume and the water-plane area, are accounted for in HydroDyn's load calculations. Among these components, diffraction, added mass, and radiation properties are imported from panel method codes as wave excitation force, added mass, and wave-radiation damping, respectively. The total external loads can be expressed with a formula consisting of three parts.

$$F_j^{Hydro} = F_j^{Waves} + \rho g V_0 \delta_{j3} - C_{jk}^{HydroStat} x_k - \int_0^t K_{jk}(t-\tau)\dot{x}_k(\tau)d\tau \tag{5}$$

The first part deals with the diffraction problem caused by incident waves. Incident waves are generated with linear waves using inverse Fourier transformations based on a selected spectrum. The forces acting on the platform, F_j^{Waves}, are then integrated using the following expression:

$$F_j^{Waves}(t) = \frac{1}{2\pi}\int_{-\infty}^{\infty} W(\omega)\sqrt{2\pi S f_\zeta^{2-sided}(\omega)}F_{Ej}(\omega,\beta)e^{i\omega t}d\omega \tag{6}$$

where t is simulation time, ω is wave frequency, β is wave direction, ζ is wave elevation, and i is the imaginary unit $\sqrt{-1}$. $Sf_\zeta^{2-sided}$ describes the power spectral density of incident waves in two-sided form. W stands for the standard normal distribution of white Gaussian noise (WGN). The variance of WGN, on average, is $\sigma_\zeta^2 = \int_{-\infty}^{\infty} Sf_\zeta^{2-sided}(\omega)d\omega$. F_{Ej} is a complex array indicating the wave-excitation force on the support platform per unit wave amplitude. Its imaginary components allow the force to be out of phase with the wave elevation. F_{Ej} is provided by panel method codes solving $F_{Ej} = -i\omega\rho\iint_{S_b} n_j\phi_D dS$, where ρ is the water density, n_j is the unit vector normal to the body surface, S_b, and ϕ_D is the diffraction potential function.

The second and third terms, $\rho g V_0 \delta_{j3} - C_{jk}^{HydroStat} x_k$, are related to the hydrostatic problem. Here, g represents the gravitational acceleration constant, V_0 is the displacement volume, and δ_{j3} denotes the Kronecker-Delta function (allowing heave direction only for the first term, following Archimedes' principle). $C_{jk}^{HydroStat}$ stands for the (j, k) component of the linear hydrostatic-restoring matrix resulting from the effects of the water-plane area and the center of buoyancy. While hydrostatic loads are independent of the wave-related hydrodynamic effects such as diffraction and radiation, they are often treated as part of the broader hydrodynamics problem for coupled dynamics analysis purposes.

The final term, $-\int_0^t K_{jk}(t-\tau)\dot{x}_k(\tau)d\tau$, is a convolution integral representing the load contribution of wave-radiation damping, B_{jk}. The final term also represents an additional contribution of frequency-depended added mass, $A_{jk}(\omega)$, not included in $A_{jk}(\infty)$. In the radiation problem, wave-radiation loads depend on the support platform's history of motion. K_{jk} represents the (j, k) component of the wave-radiation-retardation kernel matrix. τ stands for a dummy variable with the same units as the simulation time, t. HydroDyn uses hydrodynamic coefficients, A_{jk} or B_{jk}, to obtain $K_{jk}(t)$ through Fourier transformations as $K_{jk}(t) = -\frac{2}{\pi}\int_0^\infty \omega[A_{jk}(\omega) - A_{jk}(\infty)]\sin(\omega t)\,d\omega$ or $K_{jk}(t) = \frac{2}{\pi}\int_0^\infty B_{jk}(\omega)\cos(\omega t)\,d\omega$. Panel method codes provide hydrodynamic coefficients by solving, $A_{jk}(\omega) - \frac{i}{\omega}B_{jk}(\omega) = \rho\iint_{S_b} n_j\phi_k dS$. Viscous damping is not included in potential flow equations.

Consequently, time-domain simulators require panel method code outputs of hydrodynamic coefficients, A_{jk} and B_{jk}, and wave excitation force, F_{Ej}, to solve floater motions. FAST's HydroDyn module accepts data in WAMIT's output file format. While HAMS and BEMUse offer WAMIT's output format, a conversion application called BEMRosetta [42] was used for NEMOH in this study.

2.3 Response amplitude operator (RAO)

Platform motion responses to wave excitation are analyzed in the frequency domain using the response amplitude operator (RAO). RAO is a transfer function between body motion and wave amplitude, depending on wave frequency and direction. This study is carried out for head waves only, and directional effects are not addressed. Assuming linear platform motion, the equation of motion is as follows [31]:

$$[M + A(\omega)]\ddot{x} + B(\omega)\dot{x} + \left[C^{Hydro} + C^{Mooring}\right]x = F_{Exc}(\omega) = \eta F_E(\omega) \tag{7}$$

where M represents the mass and inertia matrix, and C^{Hydro} and $C^{Mooring}$ are the hydrostatic and mooring stiffness matrices. $F_{Exc}(\omega)$ denotes the excitation force while $F_E(\omega)$ is excitation force per unit wave amplitude, η. Since the linear potential flow assures linear wave theory, η is harmonic $\eta = \eta_0 \exp(i\omega t)$. Assuming $x = a\exp(i\omega t)$, RAO is defined as:

$$RAO = \frac{x}{\eta} = \frac{a}{\eta_0} = \frac{F_E(\omega)}{(C^{Hydro} + C^{Mooring}) - [M + A(\omega)]\omega^2 + i\omega B(\omega)} \tag{8}$$

RAO is a complex function. Its magnitude corresponds to platform motion responses, and its phase corresponds to the phase shift between the approaching wave and the platform response. RAOs are also estimated by spectral density analysis of motion and wave signals. The calculation procedure is as follows [43]:

$$RAO = \sqrt{(S_m(\omega)/S_w(\omega))}\, exp\left(iArg\left(S_c(\omega)\right)\right) \tag{9}$$

where $S_m(\omega)$ is the motion spectrum density, $S_w(\omega)$ is the wave spectrum density, and $S_c(\omega)$ is the cross-spectrum power density.

2.4 Evaluation metrics used in analyzing frequency-domain and time-domain differences

Compared panel method codes released at different times, each with varying levels of validation. However, the accuracy of less validated code cannot be definitively asserted. Following the methodology of [5], this study focuses on discrepancies between analyzed codes rather than experimental values. Evaluation metrics highlight agreements and disagreements. Using a statistical approach, a 5 % significance criterion was chosen to define the significance of differences, with values above the 5 % threshold deemed significant.

2.4.1 Coefficient of variation (CoV)

The coefficient of variation (CoV) is one of the evaluation metrics and was used in two ways. First, the panel method code outputs were compared at each frequency to find CoV distributions. In this way, the frequency ranges producing more divergence were determined. Then, CoV values' mean and root mean square (RMS) values were used for a more fundamental comparison based on frequency ranges. The formulas for the calculations are as follows:

$$CoV = \frac{\sigma}{\mu},\ RMS_X = \sqrt{\sum_{j=1}^{n} \frac{\left(X_j\right)^2}{n}} \tag{10}$$

In the equations, σ represents the standard deviation, μ denotes the mean, CoV stands for the coefficient of variation, and the n represents the total number of array elements.

2.4.2 Root mean square error (RMSE)

The root mean square error (RMSE) serves as another evaluation metric. Since the resultant platform motions are expressed in meters and degrees, RMSE was chosen to assess motions while maintaining units.

Maximum, RMS, and mean of resultant motions were also provided for comparability. For equations, y_j represents the values assumed true, and $\hat{y}_j$ denotes the compared values:

$$RMSE = \sqrt{\sum_{j=1}^{n} \frac{\left(\hat{y}_j - y_j\right)^2}{n}} \tag{11}$$

2.4.3 Normalized mean absolute error (NMAE) and normalized root mean square error (NRMSE)

Normalized mean absolute error (NMAE) and normalized root mean square error (NRMSE) metrics are also employed. While NRMSE highlights larger errors, NMAE treats errors equally. Both metrics yield unitless values and require reference values. The reference values were determined by comparative analysis and calculated as the Averaged results of the Remaining Three (ART) codes for any of the four panel method codes (WAMIT, NEMOH, HAMS, BEMUse). For instance, the reference values for WAMIT are calculated as $ART_{WAMIT_{Xj}} = (NEMOH_{Xj} + HAMS_{Xj} + BEMUse_{Xj})/3$. In this way, NMAE and NRMSE metrics reveal how different WAMIT results are from the others:

$$NRMSE = \frac{RMSE}{\sum_{j=1}^{n} \frac{|y_j|}{n}}, NMAE = \frac{\sum_{j=1}^{n} \frac{|\hat{y}_j - y_j|}{n}}{\sum_{j=1}^{n} \frac{|y_j|}{n}} \tag{12}$$

3. Frequency and time domain numerical models of the systems

This section describes the numerical modeling approaches for frequency and time domain simulations. First, turbine and floating platforms used in the analyses are introduced, including details on dimensions, masses, and inertia. Next, the simulation specifications and environmental conditions are given for frequency-domain and time-domain simulations. Frequency-domain analyses were carried out on a frequency range carrying significant wave energy. For time domain analyses, operational and extreme environmental conditions are used for platform motion investigations.

3.1 NREL's 5-MW baseline turbine

The NREL's 5 MW baseline turbine features a 3 m hub diameter 90 m above still water level (SWL). The rotor has a diameter of 126 m with an upwind orientation. The rotor's total mass is 110 t, and the nacelle mass is 240 t. The tower accommodating the turbine has a base diameter of 6.5 m and a mass of 249.7 t. The tower's center of mass (CM) is 43.4 m above the SWL along the tower centerline. A structural damping rate of 1 % was applied to all modes of the isolated tower. The turbine is controlled with variable speed collective pitch, and a multiple-stage gearbox is used as the drivetrain. The cut-in, rated, and cut-out wind speeds are 3 m/s, 11.4 m/s, and 25 m/s, respectively.

3.2 Platforms

Two FWT platforms were analyzed: "Hywind," a spar buoy developed by Statoil [44], and a semi-submersible developed for the DeepCWind project [45]. Modifications were made to the Hywind tower to accommodate NREL's 5 MW baseline turbine in the OC3-Hywind version [46]. The semi-submersible platform of the DeepCWind project, whose test data was used in the OC4 benchmark study, carries the same turbine and tower [47]. Both platforms are moored with three catenary lines symmetrically spread around the platforms' Z-axes. The platforms' key properties and hydrostatic and mooring stiffness coefficients are detailed in Tables 2 and 3.

3.2.1 OC3-Hywind spar buoy

The floater consists of two cylindrical bodies connected by a linearly tapered conical zone. The design incorporates a smaller diameter near the free surface to reduce hydrodynamic loads. The floater's total weight, including ballast, is 7,466 t. Including ballast, CM is located 89.92 m below the SWL along the platform's

centerline. Additional viscous drag was calculated using Morison's Equation by 100 kNs/m for surge and sway, 300 kNs/m for heave, and 13,000 kNms/rad for yaw modes. The platform has a delta connection connecting three mooring lines to increase yaw stiffness. However, the delta connection is eliminated for modeling simplification, and a yaw spring with stiffness of 98,340 kNm/rad is defined [46]. The OC3-Hywind platform is represented in schematic and discretized forms in Figure 1, where the discretized form represents only the part below SWL.

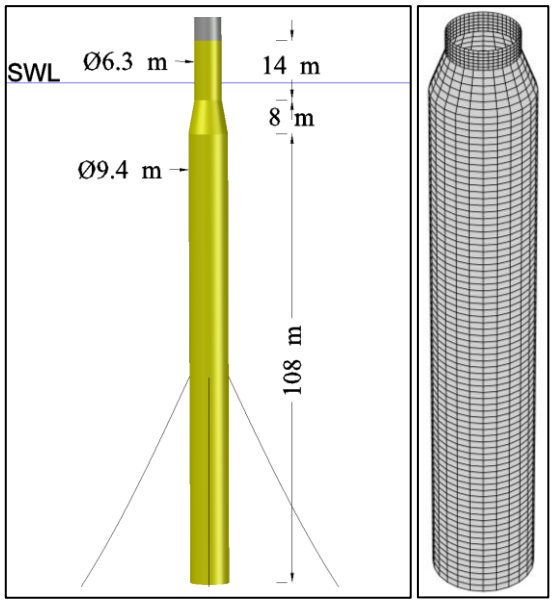

Fig. 1 Schematic view and discretized representation of OC3-Hywind spar buoy

3.2.2 OC4-DeepCWind semi-submersible

The floater features three offset columns connected to a central column through smaller diameter bracings. Larger diameter base columns at the bases of the three offset columns minimized displacement, particularly in the heave mode. The CM of the platform, including ballast, is situated 13.46 m below the SWL along the centerline. Figure 2 represents the OC4-DeepCWind platform in schematic and discretized forms, where the discretized form represents only the part below SWL, excluding bracings.

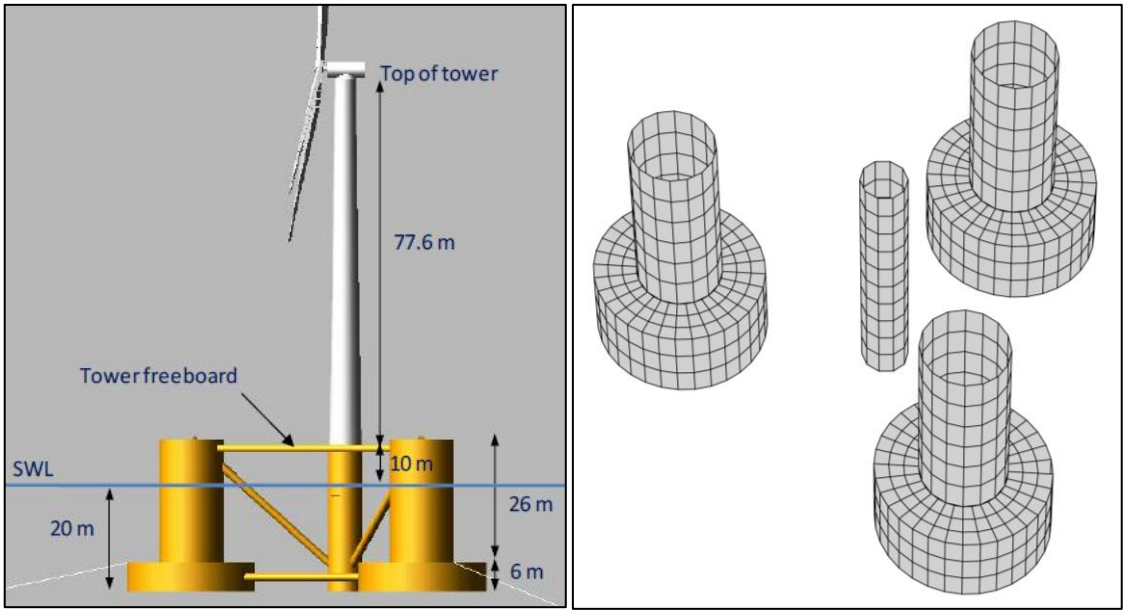

Fig. 2 Schematic view [48] and discretized representation of OC4-DeepCWind semi-submersible

Table 2 Properties of the platforms

Property	OC3-Hywind	OC4-DeepCWind
Floater type (-)	spar buoy	semi-submersible
Draft (m)	120	20
Tower freeboard (m)	10	10
Water depth (m)	320	200
Depth to fairleads below SWL (m)	70	14
Unstretched mooring line length (m)	902.2	835.5
Mooring line diameter (m)	0.0900	0.0766
The angle between adjacent lines (°)	120	120
Platform mass, including ballast (kg)	7,466,330	3,852,180
Displaced volume (m^3)	8,029	13,917
Platform CM location below SWL (m)	89.9155	13.4600
Platform Roll Inertia about CM (kgm^2)	4,229,230,000	2,561,930,000
Platform Pitch Inertia about CM (kgm^2)	4,229,230,000	2,561,930,000
Platform Yaw Inertia about CM (kgm^2)	164,230,000	4,242,650,000

Table 3 Hydrostatic and mooring stiffness coefficients of the platforms

	Modes	OC3-Hywind	OC4-DeepCWind
Hydrostatic stiffness coefficients	33 (N/m)	3.33×10^5	3.84×10^6
	44 (N m/rad)	-5.00×10^9	-3.79×10^8
	55 (N m/rad)	-5.00×10^9	-3.78×10^8
Mooring stiffness coefficients	11 (N/m)	4.12×10^4	7.08×10^4
	22 (N/m)	4.12×10^4	7.08×10^4
	33 (N/m)	1.19×10^4	1.91×10^4
	44 (N m/rad)	3.11×10^8	8.73×10^7
	55 (N m/rad)	3.11×10^8	8.73×10^7
	66 (N m/rad)	1.10×10^8	1.17×10^8
	15 (N/rad)	-2.82×10^6	-1.08×10^5
	51 (N/rad)	-2.82×10^6	-1.08×10^5
	24 (Nm/m)	2.82×10^6	1.08×10^5
	42 (Nm/m)	2.82×10^6	1.08×10^5

Note: 1=Surge, 2=Sway, 3=Heave, 4=Roll, 5=Pitch, 6=Yaw

3.3 Simulation specifications and environmental conditions

This subsection describes the simulation specifications and environmental conditions of simulated cases. First, the frequency range of the frequency-domain analyses and the solver settings are explained in the simulation specifications. Then, the environmental conditions for the time-domain simulation cases are detailed.

3.3.1 Simulation specifications

Ocean waves carry significant energy ranging from 0.04 - 0.25 Hz, depending on the location and sea state, as reported by DNV [49]. Hence, the frequency domain analysis focuses on the 0.04 - 0.25 Hz range, with 0.0016 Hz (0.01 rad/s) increments. FAST's HydroDyn employed the same range for inverse fast Fourier transformations (IFFTs) to generate incident waves. Data transfer between simulator modules used 0.01 s time steps to ensure dynamic coupling.

For both floaters, FAST models of OC3 [46] and OC4 [47] studies are available in [40]. FAST models' wind and wave generation settings were tailored to the studied environmental conditions. While significant

wave height (H_s), peak wave period (T_p), and IFFT parameters were modified, inflow wind data used for aerodynamic calculations were recreated.

System identification analyses, so-called free decay tests, are carried out to assess hydrodynamic and mooring dynamic behaviors before fully coupled dynamic tests. Free-decay tests involve no incoming waves or wind. Moreover, the tower, blades, and generator are assumed to be rigid to isolate natural frequencies from secondary effects. The moorings and six platform motion modes are the only degrees of freedom allowed. Initial displacements of 4 m, 1 m, and 4° were applied to surge, heave, and pitch modes to observe the structures' return to static equilibrium without external forces.

Fully coupled dynamic analyses were carried out once the meshes were converged and the panel method codes agreed on the natural frequencies. The investigations focused on the rated wind speed and 50-year extreme scenarios, with simulations lasting 1800 s and 11400 s, respectively. The first 600 s of each simulation were excluded to eliminate transient stages. The elimination resulted in analysis times of 1200 s (20 min) for the rated wind speed condition and 10800 s (3 h) for the extreme condition, following DNV recommendations [49].

3.3.2 Environmental conditions

The study location was selected based on the research of Li et al. [50]. Incident wind and wave conditions were created specifically for the "Norway 5" or "Site 14" location. The water depths for the platforms remained consistent (320 m for OC3-Hywind and 200 m for OC4-DeepCWind), and a seawater density of 1025 kg/m³ was used. The aerodynamics and hydrodynamics were modeled using the IEC Kaimal spectral model and the JONSWAP spectra. Wind is generated using TurbSim [51] with the IEC Kaimal spectral turbulence model. The aerodynamics modules of FAST then used the generated wind. Wind speeds at the hub height were set at 11.4 m/s for the rated wind speed and 41.86 m/s for the 50-year extreme (parked) turbine conditions. FAST's HydroDyn module generated time-domain waves using JONSWAP spectra. The rated wind speed and 50-year extreme cases have significant wave heights of 4.0 m and 13.4 m, with peak periods of 10.0 s and 13.1 s, respectively. HydroDyn determined the peak-shape parameters following the recommendations in IEC 61400-3 Annex B [52]. Simulations focused on surge, heave, and pitch modes under head waves. The properties of simulated cases are summarized in Table 4.

Table 4 Simulated cases and relevant environmental conditions in the time domain

Case definition	Turbine state	Transient time (s)	Used time (s)	Total run time (s)	Wind speed (m/s)	Significant wave height (m)	Peak wave period (s)
Free-decay	Parked	0	1800	1800	-	-	-
Rated wind speed	Rated	600	1200	1800	11.4	4.0	10.0
50-year extreme	Parked	600	10800	11400	41.86	13.4	13.1

4. Mesh sensitivity analysis

Mesh sensitivity analyses ensure consistent motion estimations across different mesh grids. The aim is to determine the grid sizes leading to convergent results for panel method code outputs. Once the appropriate meshes are determined, the resulting meshes are then employed for subsequent evaluations. The analysis also assesses each code's convergence response to grid refinements. Before the results are presented, several considerations for the analysis are explained.

The meshes of the reference benchmark studies (OC3 and OC4) were obtained from the NREL website [53]. The bracings were excluded from the OC4-DeepCWind mesh. OC3-Hywind's mesh was also modified to decrease the number of panels. Mesh independence study verifies the modified meshes and investigates how the open-source codes respond to mesh refinement. The frequency and time domain comparisons are made using the finest meshes introduced in the mesh sensitivity analysis.

4.1 Considerations

The mesh convergence study considers volumetric representation, hydrodynamic representation, and computational time cost. The criteria are discussed and satisfied throughout the mesh sensitivity analysis. Following DNV recommendations, the grid size should accurately represent the geometry. For hydrodynamic representation, DNV suggests a grid size corresponding to 1/6 of the smaller wavelength of interest for potential flow solutions [54]. While this study requires an average panel side length of 4.2 m to meet the recommendation, a maximum of 1.5 m is used in time-domain analysis. The computational time cost is also essential. Coarser meshes lead to faster solutions but may sacrifice precision due to reduced volumetric and hydrodynamic representation. On the other hand, refining the mesh increases processing time. Therefore, mesh convergence studies require balancing between precision and processing time.

4.1.1 OC3-Hywind spar-buoy mesh

The OC3 benchmark mesh was modified to decrease the number of panels. A local refinement was applied to the upper cylinder of OC3-Hywind, considering the wave excitation zone's proximity to the free surface. At the upper cylinder, the grid size was kept at half the size of the remaining part. Finally, the finest mesh was determined with approximately 4000 panels.

4.1.2 OC4-DeepCWind semi-submersible mesh

For the OC4-DeepCWind platform, the original OC4 benchmark study mesh was employed by excluding the bracings. The exclusion was necessary due to the challenges posed by the mesh refinement of the slender bracing geometry. Indeed, the bracings have minimal impact on the overall hydrodynamic behavior in the time domain, as shown by Uzunoglu and Guedes Soares [55].

4.1.3 Mesh refinement process

Once the finest meshes are established, coarser meshes are generated while preserving the rationale for local refinements. Four meshes - finest, fine, coarse, and coarsest - were created to indicate their relative refinement levels. The NMAE metric was used for the mesh sensitivity analysis. The reference values for NMAE were defined as the results of each code's finest meshes, serving as the basis for normalization. Referencing the finest meshes allows for quantifying the performance of coarser meshes relatively. The convergence of each code to refinement is briefly illustrated in separate figures. Variations based on panel number are also presented to assess the computational time costs per wave period per panel number square. For reference, the simulations were performed on a 14-core i7-1370P CPU running at 5.20 GHz.

4.2 Panel method code responses to mesh refinement

The mesh convergence study considered volumetric representation, hydrodynamic representation, and computational time cost. Volumetric representation improved as the number of prism faces increased, but the effectiveness diminished beyond a certain point. The coarsest meshes yielded more than 90 % of the analytically calculated volume, and the finest meshes provided around 99 %. The volume difference between the fine and finest meshes was approximately 0.5 % for both platforms, which is consistent with similar studies on panel methods [56-58] and satisfies the volumetric representation criterion. Hence, refinements beyond the finest meshes have minimal impact on frequency domain results. The average panel side lengths for the finest meshes were 1 m for OC3-Hywind and 1.5 m for OC4-DeepCWind. Mesh properties are given in Table 5.

Table 5 Mesh properties

		Min/Max grid sizes (m)		Normalized volume (%)		Panel numbers	
Mesh definitions	Mesh labels	OC3-Hywind	OC4-DeepCWind	OC3-Hywind	OC4-DeepCWind	OC3-Hywind	OC4-DeepCWind
Coarsest	M1	1.1/4.3	3.3/6.0	90.12	90.38	288	198
Coarse	M2	0.8/2.7	2.4/3.8	95.53	95.91	664	594
Fine	M3	0.4/1.2	1.4/2.4	98.87	98.41	2292	1430
Finest	M4	0.3/1.0	1.1/1.5	99.36	98.96	4042	2376

4.2.1 Computational efficiency

Codes exhibited different responses to mesh refinement, and the order of time requirement varied with the mesh number. Computational time cost increases quadratically with the number of panels for the same number of frequencies requested. Thus, for simplicity in comparison, the computational time costs are normalized with the number of frequencies and the square of panel numbers. The time requirement order may change beyond the studied mesh numbers. However, the range of mesh numbers investigated in this study might be sufficient for most FWT platforms, considering DNV's grid size recommendations.

In Figure 3, HAMS and BEMUse performed faster due to their utilization of multicore processing, unlike WAMIT (due to the version used) and NEMOH. For the 4042 panel numbers, HAMS was 12, 9, and 1,5 times faster than WAMIT, NEMOH, and BEMUse. All the codes performed less efficiently for mesh numbers below 500, which is more prominent for OC4-DeepCWind. The reason might be primarily due to the slower initialization processes of the codes. Beyond the initialization effect, trends exhibited by codes are horizontal for HAMS and BEMUse, increasing for WAMIT, and decreasing for NEMOH. The codes performed almost the same for OC3-Hywind and OC4-DeepCWind platforms.

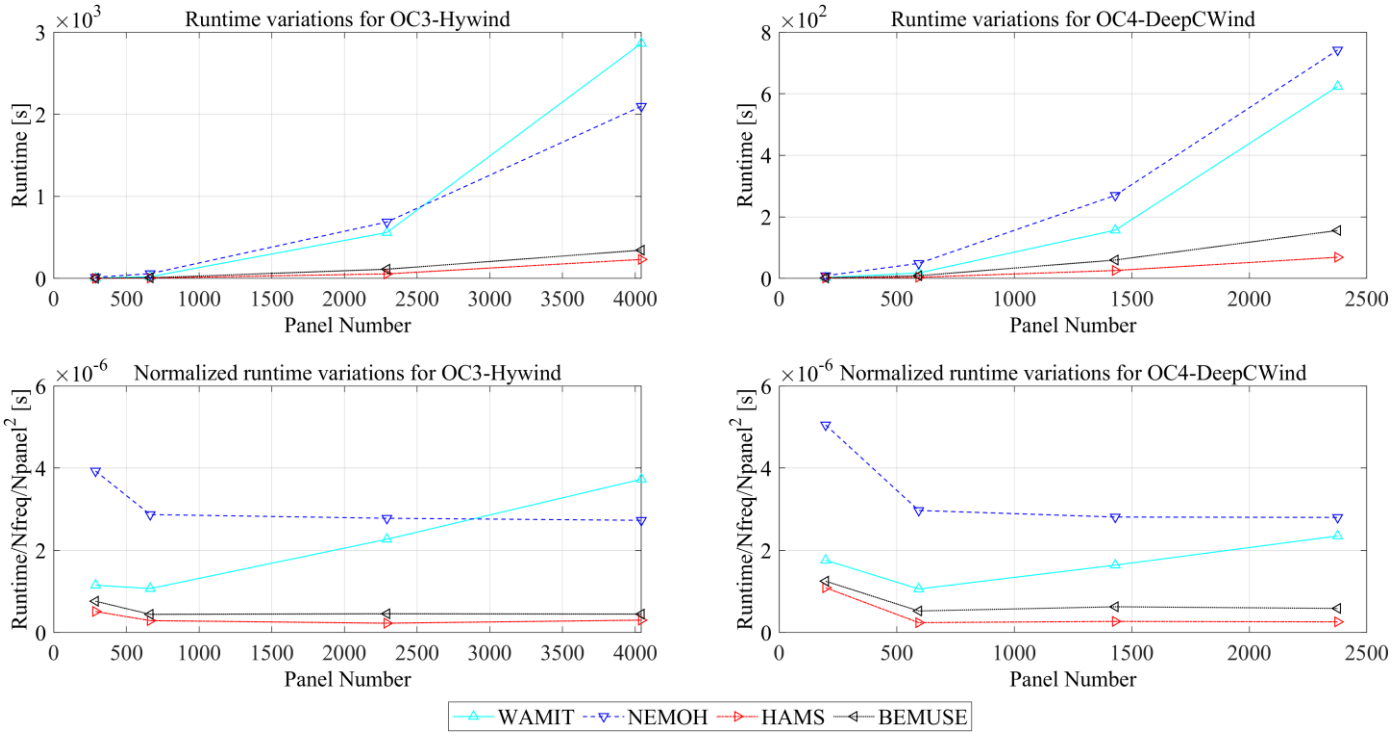

Fig. 3 Computational efficiencies of the panel method codes. Nfreq: number of frequencies, Npanel: number of panels

4.2.2 Convergence analysis

The NMAE results are summarized for the modes relevant to head waves, i.e., surge, heave, and pitch. NMAE values of each mesh's added mass, (A), radiation damping, (B), and wave excitation forces, (F_{E}), were normalized by the finest mesh results. Then, the mode-averaged results were obtained by averaging the normalized values of A, B, and F_{E}. For instance, normalized NMAE values for the surge mode (1) of A_{11}, B_{11}, and F_{E1} were averaged and designated as mode-averaged Surge results, $\mathrm{Surge} = (A_{11} + B_{11} + F_{\mathrm{E1}})/3$. Similarly, variable-averaged results (for A, B, and F_{E}) were also summarized by averaging the examined modes of surge, heave, and pitch. For example, added mass results were summarized as taking the average of NMAE values for surge (1), heave (3), and pitch (5) modes, $A = (A_{11} + A_{33} + A_{55})/3$. By this method, only three variables and three modes are analyzed instead of nine, which are A_{11}, A_{33}, A_{55}, B_{11}, B_{33}, B_{55}, F_{E1}, F_{E3}, and F_{E5}.

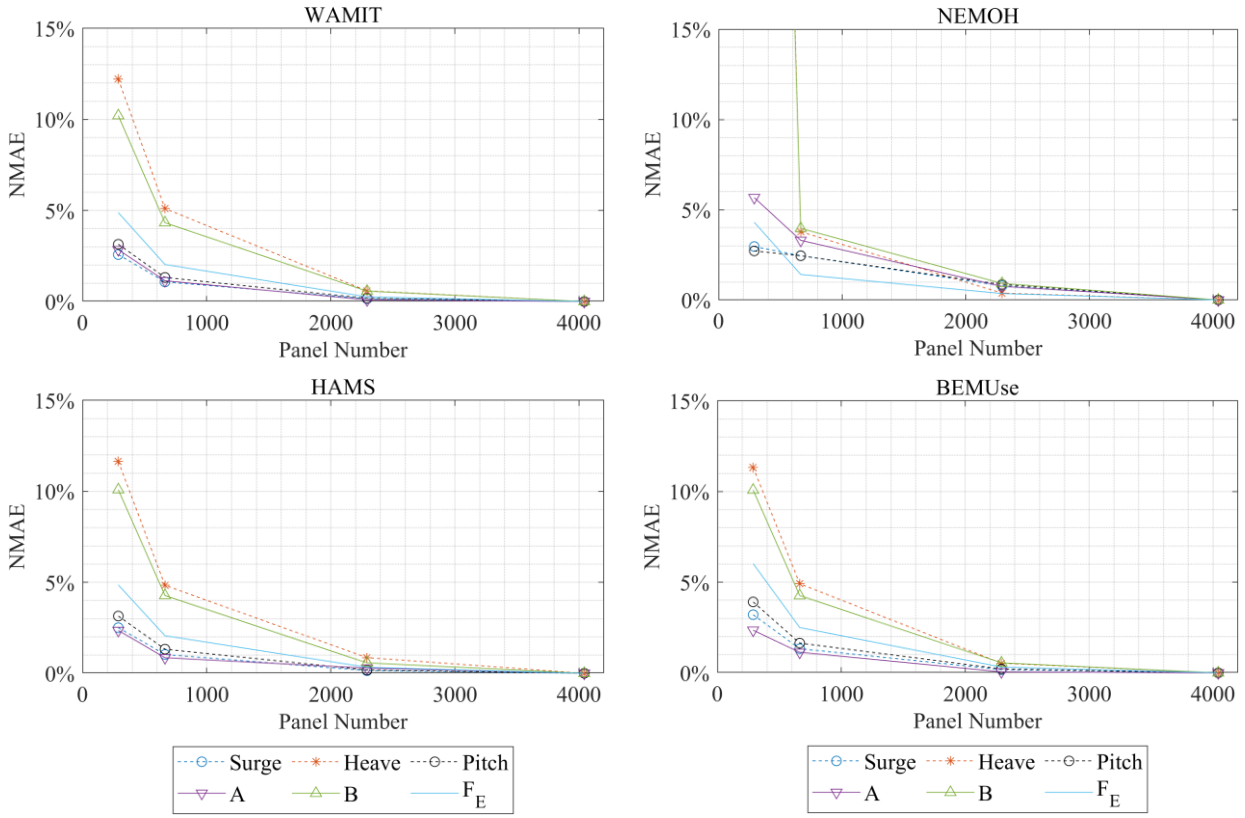

Fig. 4 NMAE metric results for the OC3-Hywind spar buoy

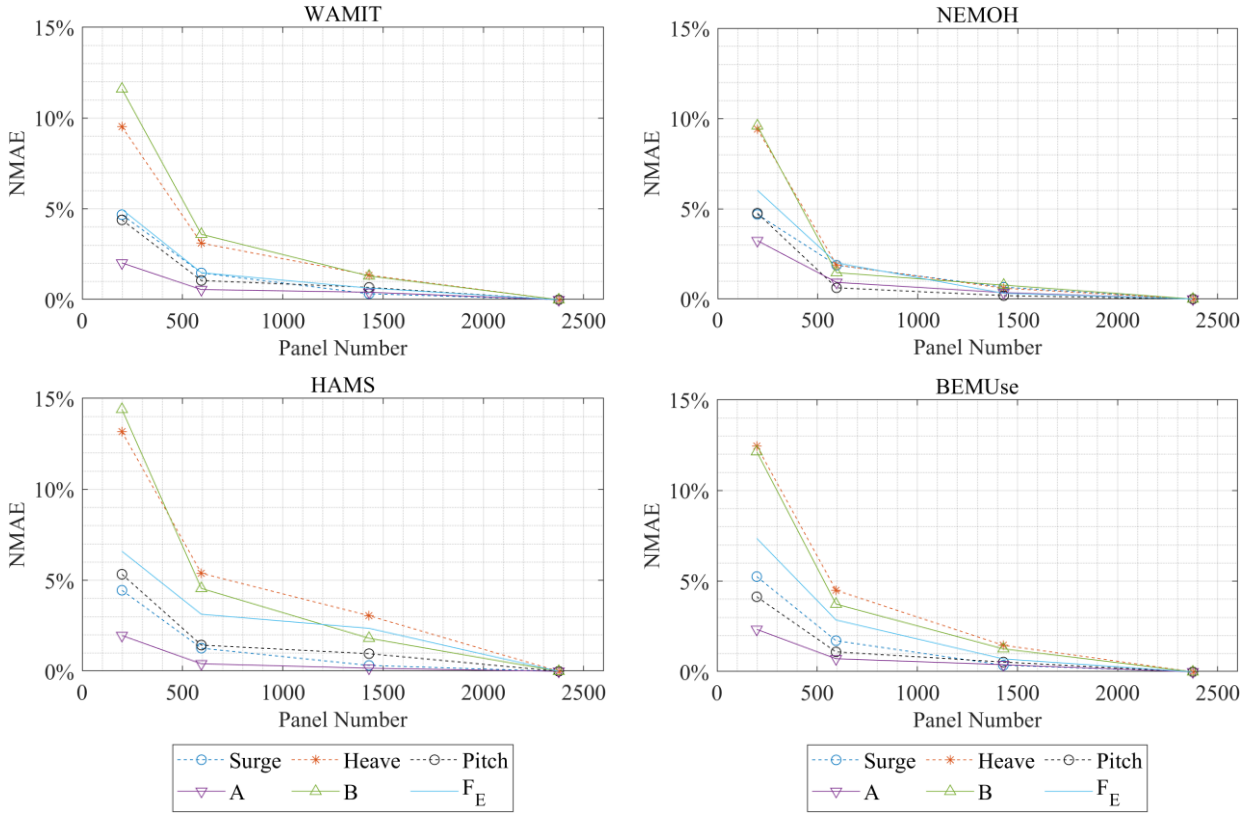

Fig. 5 NMAE metric results for the OC4-DeepCWind semi-submersible

Overall, mesh refinement results showed convergence and provided insights into each code's computational efficiency. The finest meshes were used as references for the NMAE metric. The highest NMAE results for both platforms did not exceed 3 % for the fine meshes, indicating mesh independence and

satisfying the hydrodynamic representation criterion. Once the volumetric and hydrodynamic representation criteria are satisfied, the refinement process is stopped to satisfy the computational time cost criterion.

For OC3-Hywind, Figure 4 shows the responses of panel method codes to the mesh refinement. For an average of all studied values, the highest and lowest average NMAE values belonged to NEMOH and HAMS for the coarsest and coarse meshes. For fine mesh, those were NEMOH and BEMUse.

For OC4-DeepCWind, Figure 5 shows the responses of the panel method codes to the mesh refinement process. For an average of all studied values, the highest and lowest average NMAE values belonged to HAMS and NEMOH for each mesh.

For both platforms, HAMS converged the slowest, and NEMOH converged the fastest. Overall, the highest NMAE values were in heave mode and radiation damping results, and the lowest NMAE values were in surge mode and added mass results. Consequently, the most mesh-sensitive results belonged to the heave radiation damping, B_{33}, and the least mesh-sensitive results belonged to the surge added mass, A_{11}.

5. Comparison of hydrodynamics in the frequency-domain

This section evaluates the discrepancies between panel method code outputs using evaluation metrics for the finest meshes. The significance of the differences was primarily assessed through the coefficient of variation results. For further analysis, each code was compared against the average of the remaining three codes using NRMSE and NMAE metrics.

Figures 6 and 7 present the results of OC3-Hywind and OC4-DeepCWind for added mass, radiation damping, wave excitation force, response amplitude operator, and coefficient of variation. Only the results for the surge (1), heave (3), and pitch (5) modes are shown due to heading waves and floater symmetries. The results are represented in dimensionless-unitless forms for standardization. For nondimensionalization, seawater density (ρ), gravitational acceleration (g), angular frequency (ω), and a length scale (L) were used to normalize added mass ($A/\rho L^m$), potential damping ($B/\rho\omega L^m$), and excitation forces ($F_E/\rho g L^m$). For added mass and radiation damping, the exponent m equals 3 for surge and heave modes and equals 5 for pitch mode. For excitation forces, m equals 2 for surge and heave modes and 3 for pitch mode. Dimensional values can be obtained by multiplying the presented results with proper denominators. The length scale used in this study is 1 m.

The NRMSE and NMAE results of A, B, F_{E}, and RAO are given in Tables 6 and 9 for OC3-Hywind and OC4-DeepCWind, respectively. Table 7 presents the RMS of CoV values for A, B, F_{E}, and RAO. Additionally, Table 8 tabulates non-dimensional infinite frequency added mass results.

Overall, there was a close agreement among panel method codes for the OC3-Hywind spar buoy except for NEMOH. The codes agreed less for the OC4-DeepCWind semi-submersible; however, most discrepancies remained below the 5 % significance criterion threshold.

5.1 OC3-Hywind spar buoy

5.1.1 Surge mode

In surge mode, NEMOH is noticeably separated from the others. However, the CoV values of any examined variables, A_{11}, B_{11}, F_{E1}, and RAO_1, did not exceed the 5 % significance criterion threshold for any frequency. Only the surge radiation damping, B_{11}, results for NEMOH-ART exceeded the 5 % threshold for the NRMSE and NMAE results. Due to the scale of the *y*-axis, observation of the figures alone may be misleading. For comparability, the NRMSE and NMAE results of A_{11} are smaller than those of B_{11}.

5.1.2 Heave mode

In heave mode, the RMS of CoV exceeded 5 % for heave radiation damping, B_{33}. However, excluding only 0.04 Hz results of B_{33} reduced the RMS of CoV below 5 %. BEMUse separated from the others for RAO_3 lower than 0.05 Hz, which was indicated by the NRMSE metric with a value higher than 10 %. Since

NRMSE highlights larger differences, a relatively high NRMSE - low NMAE situation was observed for BEMUse RAO_3 results.

5.1.3 Pitch mode

In pitch mode, the RMS of CoV for radiation damping, B_{55}, exceeded the 5 % significance criterion threshold due to NEMOH's separation in a wide range. This discrepancy was also quantified with NRMSE and NMAE results that were higher than 10 % for NEMOH. For frequencies less than 0.05 Hz, BEMUse differed from the others for RAO_5, similar to other modes.

5.1.4 Infinite frequency added-mass results

For the OC3-Hywind platform, examined panel method codes produced almost the same results for the infinite frequency added mass results, except for NEMOH. Parallel to its results in the studied frequency range, NEMOH separated from the others for the infinite frequency results in the surge and pitch mode. If NEMOH is not considered, CoV values fall below 0.01 %.

Table 6 NRMSE and NMAE for OC3-Hywind spar buoy

Panel Method Code	Metric	*A*			*B*			F_E			RAO		
		11	33	55	11	33	55	1	3	5	1	3	5
WAMIT-ART	NRMSE (%)	1.2	0.1	1.2	2.3	0.8	3.7	0.5	0.4	0.6	0.8	3.4	0.6
	NMAE (%)	1.2	<0.1	1.2	1.9	0.7	3.4	0.5	0.1	0.5	0.3	0.7	0.3
NEMOH-ART	NRMSE (%)	3.7	0.1	3.6	6.4	2.2	11.5	1.7	0.3	2.4	0.6	3.2	2.3
	NMAE (%)	3.7	0.1	3.6	5.5	2.0	10.5	1.6	0.1	1.9	0.2	0.7	1.2
HAMS-ART	NRMSE (%)	1.2	0.1	1.2	1.6	0.7	3.6	0.4	0.4	0.6	0.8	3.6	0.6
	NMAE (%)	1.2	0.1	1.2	1.3	0.6	3.3	0.3	0.2	0.5	0.3	0.8	0.3
BEMUse-ART	NRMSE (%)	1.2	0.1	1.2	2.5	0.7	3.8	1.0	1.1	1.7	2.2	10.3	2.9
	NMAE (%)	1.2	0.1	1.2	2.1	0.7	3.5	0.9	0.3	1.0	0.6	2.1	1.0

Note: 1-Surge, 3-Heave, 5-Pitch

Table 7 RMS of CoV values for WAMIT-NEMOH-HAMS- BEMUse outputs

Platform	*A* (%)			*B* (%)			F_E (%)			RAO (%)		
	Surge	Heave	Pitch	Surge	Heave	Pitch	Surge	Heave	Pitch	Surge	Heave	Pitch
OC3-Hywind	1.8	0.1	1.8	2.8	6.1 – 3.0	6.1	0.9	2.6 – 1.2	1.0	0.4	2.6 – 1.2	0.5
OC4-DeepCWind	1.5	1.4	1.1	2.9	99.4 – 19.4	3.7	1.4	15.9 – 8.6	4.7	1.3	16.5 – 10.0	4.7

Note: The first number covers the entire range for cells with a dash between two numbers, while the second excludes 0.04 Hz results for OC3-Hywind and 0.0625 Hz to 0.0745 Hz for OC4-DeepCWind.

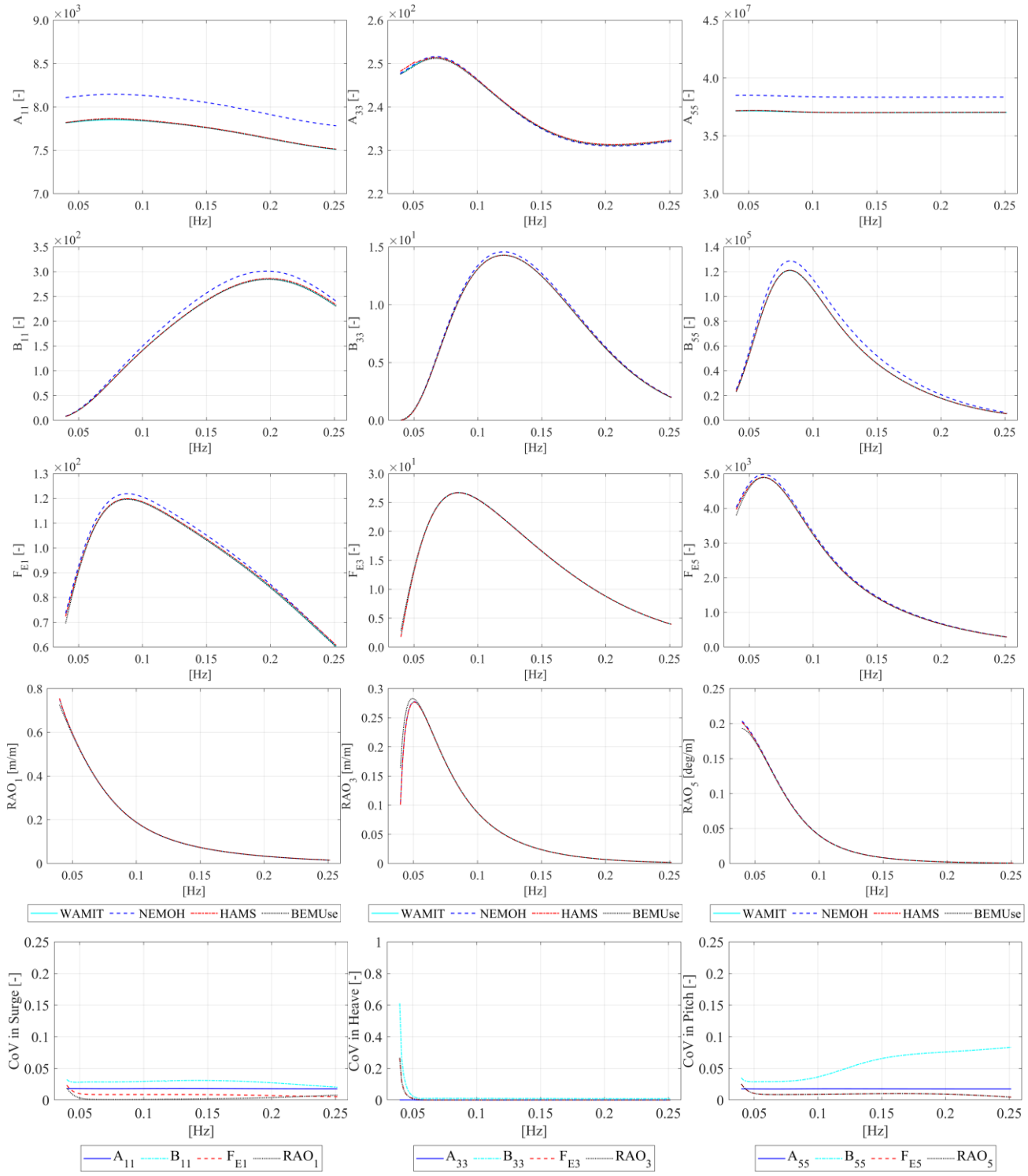

Fig. 6 Non-dimensional added mass (A), radiation damping (B), wave excitation force (F_E), response amplitude operator (RAO), and coefficient of variation (CoV) results of OC3-Hywind for surge (1), Heave (3), and Pitch (5)

5.2 OC4-DeepCWind semi-submersible

5.2.1 Surge mode

In surge mode, there was a close agreement. The 5 % significance criterion threshold is exceeded only by the NRMSE results of NEMOH and BEMUse for B_{11} and RAO_1, respectively. The reason for NEMOH was its local separation from the others around the peak value of radiation damping, B_{11}, near 0.17 Hz. The reason for BEMUse was its divergence in the response amplitude operator, RAO_1, for frequencies less than

0.05 Hz. BEMUse's divergence resulted in CoV values exceeding the 5 % threshold below 0.05 Hz. Nevertheless, the RMS of CoV remained below 5 % for the entire range.

5.2.2 Heave mode

The heave mode exhibited significant discrepancies, particularly for radiation damping, B_{33}. High CoV values in B_{33} were observed in some ranges where the codes produced negative and positive numbers, leading to mean values approaching zero. As a disadvantage of the CoV metric, the CoV tends towards infinity when the mean value is close to zero. However, the negative damping values only constituted around 5 % of the studied range, from 0.0625 Hz to 0.0745 Hz. Excluding this range reduced the RMS of CoV results significantly, as given in Table 7. Additionally, some high CoV values were noted for the heave mode in the 0.20 Hz - 0.25 Hz range, where HAMS separated from others for B_{33} and F_{E3}. Nonetheless, as RAO_3 values were close to zero within this range, differences had minimal impact on platform motion.

For A_{33}, the codes exhibited a high agreement. Only NEMOH separated from the others insignificantly, i.e., none of the evaluation metric results exceeded the 5 % significance threshold.

For B_{33} results, the codes disagreed the most. NRMSE and NMAE results of all codes exceeded the 5 % significance criterion threshold. One reason is NEMOH's significantly lower results between 0.10 Hz - 0.12 Hz and 0.16 Hz - 0.20 Hz. The other reason is HAMS's detached peak of about 0.21 Hz, which results in a relatively high NRMSE - low NMAE.

For F_{E3}, HAMS exceeded the significance criterion threshold for the NMAE due to its separation from others in the 0.04 Hz - 0.06 Hz and 0.20 Hz - 0.22 Hz ranges. A relatively high NRMSE - low NMAE was observed for HAMS due to its detached peak of about 0.21 Hz, similar to B_{33}.

The shape of the RAO_3 CoV values was parallel to F_{E3}, except for an additional peak, which should be addressed to the resonance [59]. Motion identification becomes challenging around structures' natural frequencies, as indicated by a relatively high NRMSE - low NMAE. Resonance was only observed in the OC4-DeepCWind in the heave mode since the other natural frequencies were out of the investigated range.

5.2.3 Pitch mode

In pitch mode, CoV results exhibited local peaks at 0.16 Hz and 0.24 Hz for F_{E5} and RAO_5, coinciding with the local and global minima. The CoV peaks did not cause the CoV RMS to exceed 5 % and had no significant impact on platform motions since the corresponding RAO_5 values are below 0.1. For the NRMSE and NMAE results, only NEMOH's B_{55} results exceeded the 5 % threshold due to its separation between 0.10 Hz and 0.15 Hz.

5.2.4 Infinite frequency added-mass results

Panel method codes agree with the infinite frequency added mass results for OC4-DeepCWind, except for NEMOH. Excluding NEMOH, the CoV values are below 0.5 %. Additionally, without considering HAMS's heave and pitch mode results along with NEMOH, the CoV values drop below 0.1 %.

Table 8 Non-dimensional infinite frequency added mass results

Platform	Mode	WAMIT	NEMOH	HAMS	BEMUse	CoV (%)
OC3-Hywind	11	7.57×10^3	7.85×10^3	7.57×10^3	7.57×10^3	1.59
	15	-4.72×10^5	-4.89×10^5	-4.72×10^5	-4.72×10^5	-1.55
	33	2.37×10^2	2.37×10^2	2.37×10^2	2.37×10^2	0.00
	55	3.70×10^7	3.84×10^7	3.70×10^7	3.70×10^7	1.62
OC4-DeepCWind	11	6.17×10^3	6.36×10^3	6.16×10^3	6.17×10^3	1.35
	15	-8.10×10^4	-8.23×10^4	-8.08×10^4	-8.09×10^4	-0.75
	33	1.40×10^4	1.37×10^4	1.41×10^4	1.40×10^4	1.08
	55	7.03×10^6	6.89×10^6	7.06×10^6	7.03×10^6	0.94

Note: 1-Surge, 3-Heave, 5-Pitch.

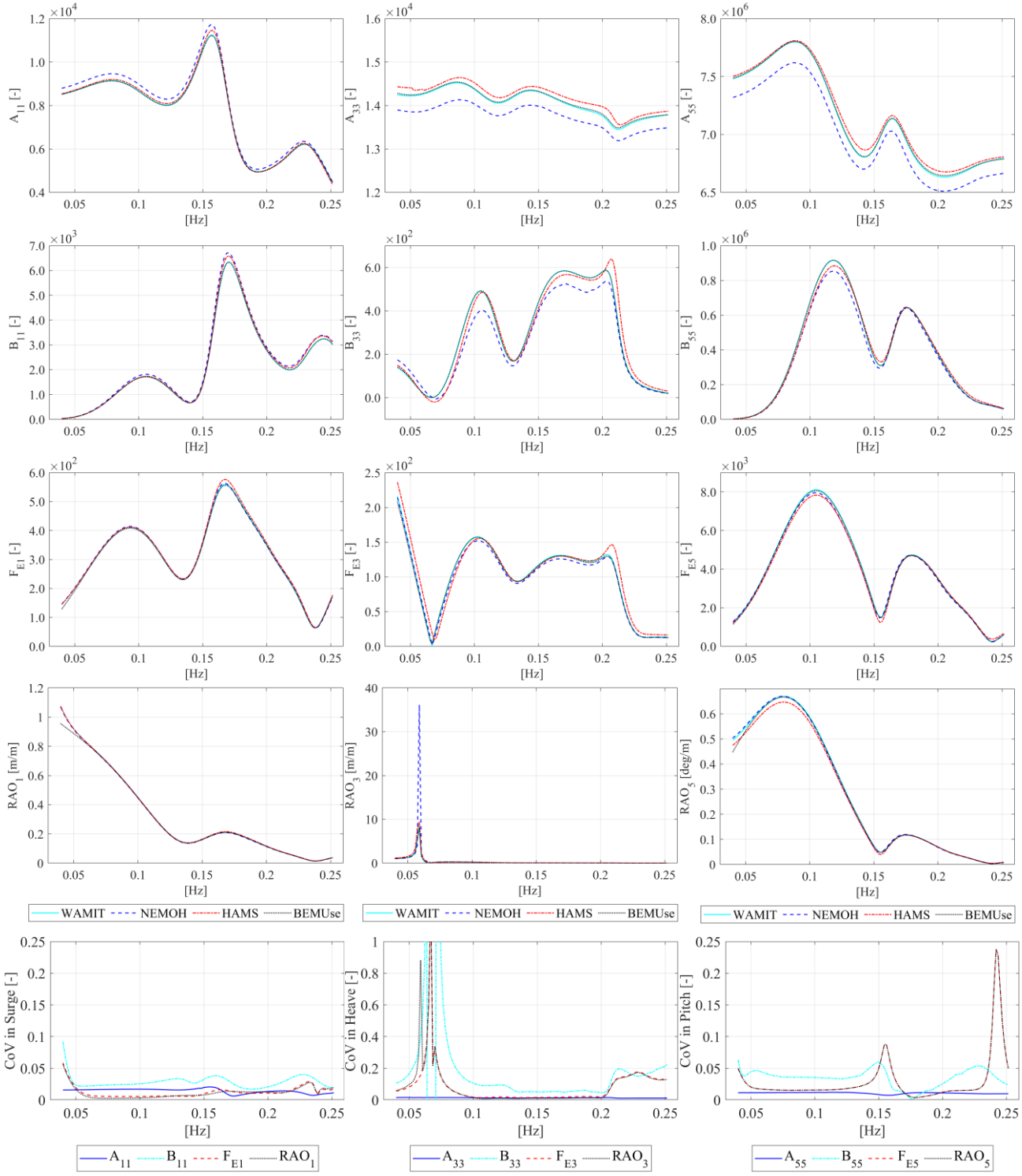

Fig. 7 Non-dimensional added mass (A), radiation damping (B), wave excitation force (F_E), response amplitude operator (RAO), and coefficient of variation (CoV) results of OC4-DeepCWind for Surge (1), Heave (3), and Pitch (5)

In summary, except for NEMOH's radiation damping results, the examined codes showed close agreement for surge and pitch modes on both platforms. While heave mode results for OC3-Hywind also exhibited close agreement, there were significant differences in OC4-DeepCWind results. These differences were notable in the most mesh-sensitive results of the mesh convergence study, particularly in the heave mode and radiation damping. The highest NMAE results for OC4-DeepCWind were around 3 %, and for OC3-Hywind, those were less than 1 %. Hence, NMAE values of less than 1 % are recommended for better agreement among panel method codes.

Table 9 NRMSE and NMAE for OC4-DeepCWind semi-submersible.

Panel Method Code	Metric	A			B			F_E			RAO		
		11	33	55	11	33	55	1	3	5	1	3	5
WAMIT-ART	NRMSE (%)	1.3	0.4	0.5	3.9	7.4	2.9	0.7	3.7	2.3	2.0	201	2.4
	NMAE (%)	1.1	0.4	0.5	2.8	6.0	2.0	0.5	3.1	1.8	0.7	20.9	1.8
NEMOH-ART	NRMSE (%)	3.2	2.7	2.1	6.0	15.5	6.3	1.0	4.2	1.8	1.6	732	1.9
	NMAE (%)	2.9	2.6	2.1	4.6	12.6	4.6	0.9	3.8	1.5	0.8	72.8	1.4
HAMS-ART	NRMSE (%)	0.6	1.7	1.1	2.4	15.9	3.9	2.0	11.2	3.3	2.1	205	4.1
	NMAE (%)	0.6	1.6	1.1	1.5	8.3	3.0	1.5	7.7	2.8	1.2	33.0	3.1
BEMUse-ART	NRMSE (%)	1.6	0.6	0.6	3.9	7.6	3.1	1.7	5.5	1.6	5.3	223	1.9
	NMAE (%)	1.4	0.6	0.6	2.8	6.3	2.2	1.4	3.7	1.3	1.7	25.3	1.3

Note: 1-Surge, 3-Heave, 5-Pitch

6. Coupled dynamics in time-domain and motion analysis

This section analyses the time-domain simulator results fed from studied panel method codes. The section starts with system identification analysis, examining hydro and mooring dynamics while turning off aero-servo-elasto dynamics. Next, the resultant motion dynamics are evaluated for two environmental conditions: the rated wind speed and 50-year extreme cases. Then, the distribution of differences across wave frequencies is investigated using power spectral density (PSD) and RAO. Finally, a filtering process is carried out to focus on the first-order wave excitation range, and the results before and after filtering are compared.

6.1 System identification analyses

Free-decay tests identifying the system enabled only hydro-elasto-mooring dynamics, i.e., disabled the aero and servo dynamics. The results fed from studied panel method codes exhibited close agreement except for NEMOH's phase shifts. The phase shifts are due to the discrepancies in hydrodynamic coefficients and are hardly discernable in Figure 8. Moreover, there was an excellent agreement for all natural frequencies except surge mode result fed by NEMOH for OC3-Hywind. The discrepancy is mainly due to the infinite frequency added mass result differences between NEMOH and the other codes. Table 10 summarizes the natural frequencies of panel method code outputs.

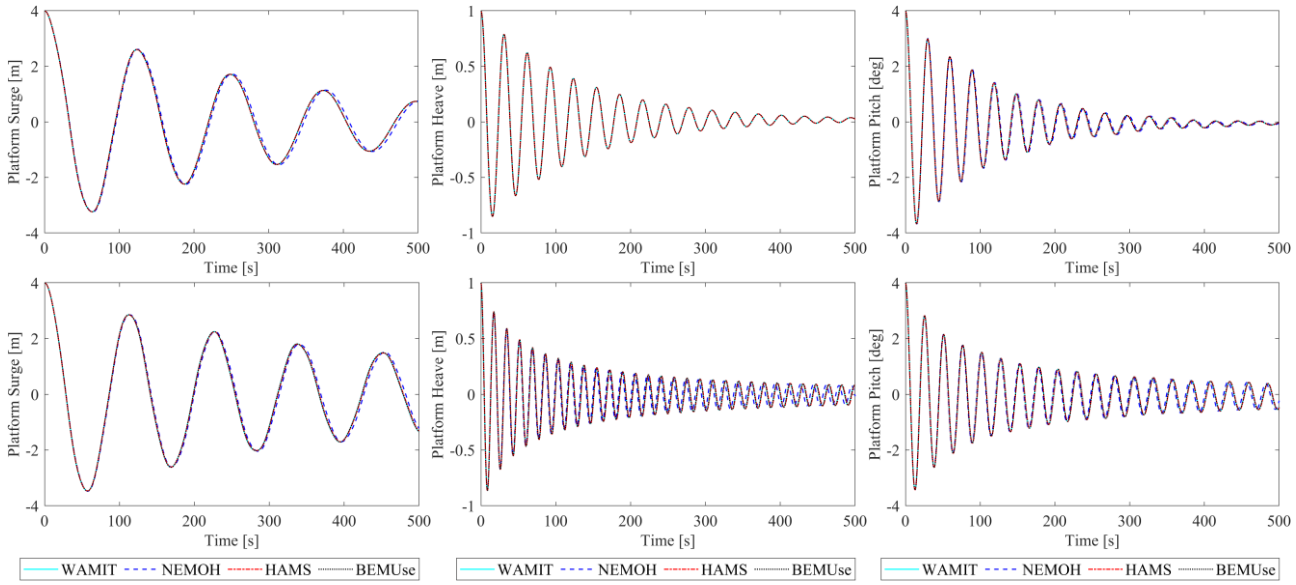

Fig. 8 Free Decay motions for OC3-Hywind (up) and OC4-DeepCWind (down)

Table 10 Natural frequencies from free decay analysis

Platform	Variable	Surge (Hz)	Heave (Hz)	Pitch (Hz)
OC3-Hywind spar buoy	WAMIT	0.0083	0.0322	0.0339
	NEMOH	0.0078	0.0322	0.0339
	HAMS	0.0083	0.0322	0.0339
	BEMUse	0.0083	0.0322	0.0339
	CoV (%)	2.9	0.0	0.0
OC4-DeepCWind semi-submersible	WAMIT	0.0089	0.0583	0.0394
	NEMOH	0.0089	0.0583	0.0394
	HAMS	0.0089	0.0583	0.0394
	BEMUse	0.0089	0.0583	0.0394
	CoV (%)	0.0	0.0	0.0

6.2 Resultant-motion based analyses

In this subsection, platform motion results in the time domain fed by the studied panel method codes are evaluated. The motion results can be interpreted dimensionally since the values are in meters and degrees. Therefore, the root mean square error metric was used to analyze the differences between motion results dimensionally. The maximum, mean, and RMS values of the motions might be used as references of RMSE.

Figure 9 illustrates the OC3-Hywind surge platform motion for the rated wind speed case. Despite zooming in, the discrepancies are barely discernible. Hence, the remaining resultant motions are presented solely in tabular format to represent the distributions of deviations clearly.

Tables 11 and 12 show the summary statistics for the resultant motions of OC3-Hywind and OC4-DeepCWind, respectively. The tables include the maximum, RMS, and mean values of the resultant motions and the corresponding coefficient of variation values to highlight differences. Furthermore, the RMSE, NRMSE, and NMAE metrics present the discrepancies with a relative approach. The mean values given here were calculated as a mean of absolute $\sum_{i=1}^{n} \frac{|y_i|}{n}$. The same formula was used for reference mean calculations of NRMSE and NMAE metrics, as shown in Equation 12.

For the rated wind speed cases, summarized differences are within centimeters and below unit degrees, indicating close agreement among panel method codes. Besides, the results of the evaluation metrics are below the 5 % significance criterion threshold, with an exception. The exception is in the heave mode results of OC4-DeepCWind, which have motion results close to zero, increasing the deviation.

For 50-year extreme cases, deviations were higher than rated wind speed cases due to longer simulation times and extreme environmental conditions. Nevertheless, considering the motion range and environmental conditions, discrepancies between the resultant motion estimations remained limited.

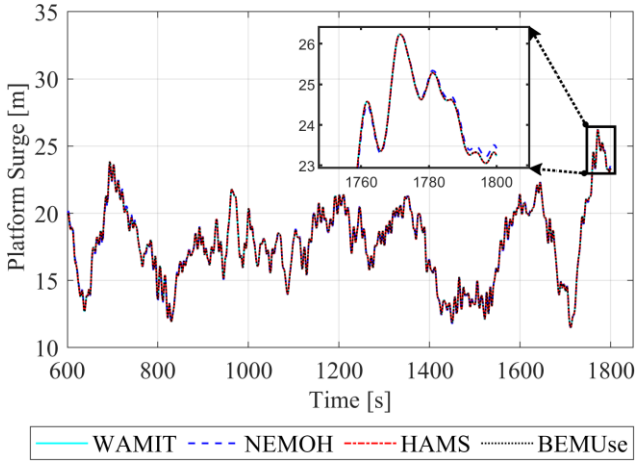

Fig. 9 Platform motions of OC3-Hywind in surge mode for rated wind speed case

6.2.1 OC3-Hywind spar buoy

For the rated wind speed case, the highest CoV value belonged to maximum motion in heave mode results and was below 0.5 %, and the remaining CoV values were below 0.05 %. The highest NRMSE value of 1.3 % corresponds to an RMSE of less than 0.01 m, and the highest RMSE of 0.09 m corresponds to 0.5 % NRMSE.

For the 50-year extreme case, the highest CoV value belonged to maximum motion in pitch mode results and was below 0.2 %, and the other CoV values remained below 0.1 %. The highest NRMSE value of 0.6 % corresponds to an RMSE of less than 0.01 m, and the highest RMSE of 0.03 m corresponds to 0.3 % NRMSE.

Table 11 Time-domain results of OC3-Hywind spar buoy fed from compared panel method codes

		Rated wind speed case			50-year extreme case		
Value	Panel Method Code	Surge (m)	Heave (m)	Pitch (°)	Surge (m)	Heave (m)	Pitch (°)
Maximum	WAMIT	26.24	0.91	6.08	17.65	2.36	6.00
	NEMOH	26.23	0.92	6.08	17.61	2.36	5.98
	HAMS	26.24	0.91	6.08	17.65	2.36	6.00
	BEMUse	26.24	0.91	6.08	17.63	2.36	5.99
	CoV (%)	0.02	0.43	0.00	0.09	0.04	0.14
RMS	WAMIT	17.97	0.39	3.83	9.24	0.69	1.99
	NEMOH	17.97	0.39	3.83	9.24	0.69	1.99
	HAMS	17.97	0.39	3.83	9.24	0.69	1.99
	BEMUse	17.97	0.39	3.83	9.24	0.69	1.99
	CoV (%)	0.00	0.00	0.00	0.02	0.00	0.08
Mean	WAMIT	17.74	0.35	3.69	8.89	0.56	1.68
	NEMOH	17.74	0.35	3.69	8.89	0.56	1.67
	HAMS	17.74	0.35	3.69	8.89	0.56	1.68
	BEMUse	17.74	0.35	3.69	8.89	0.56	1.67
	CoV (%)	0.00	0.00	0.01	0.01	0.00	0.05
RMSE	WAMIT-ART	0.03	<0.01	<0.1	0.01	<0.01	<0.1
	NEMOH-ART	0.09	<0.01	<0.1	0.03	<0.01	<0.1
	HAMS-ART	0.03	<0.01	<0.1	0.01	<0.01	<0.1
	BEMUse-ART	0.03	<0.01	<0.1	0.01	<0.01	<0.1
NRMSE (%)	WAMIT-ART	0.2	0.4	0.2	0.1	0.2	0.2
	NEMOH-ART	0.5	1.3	0.4	0.3	0.6	0.5
	HAMS-ART	0.2	0.4	0.1	0.1	0.2	0.2
	BEMUse-ART	0.2	0.4	0.1	0.1	0.3	0.2
NMAE (%)	WAMIT-ART	0.1	0.4	0.1	0.1	0.1	0.2
	NEMOH-ART	0.4	1.1	0.3	0.2	0.2	0.4
	HAMS-ART	0.1	0.3	0.1	0.1	0.1	0.2
	BEMUse-ART	0.1	0.4	0.1	0.0	0.2	0.1

6.2.2 OC4-DeepCWind semi-submersible

For the rated wind speed case, the CoV values for maximum, RMS, and mean were under 0.5 %, except for the heave mode, for which the range of motion is small. The evaluation metrics are highly sensitive for values close to zero, such as in the heave mode. The highest NRMSE value was also in the heave mode, with 19.7 %, corresponding to only 0.03 m for RMSE. Besides, the highest RMSE of 0.06 m corresponds to 0.8 % NRMSE.

For the 50-year extreme case, the maximum, RMS, and mean CoV values remained under 1.5 %, except for the heave mode. All the heave mode results of NRMSE and NMAE exceeded the 5 % significance criterion

threshold due to discrepancies in the hydrodynamic coefficients. Maximum heave motions were around 4 - 4.5 meters, with RMSE results under 8 cm except for HAMS (19 cm RMSE). The higher RMSE of the time domain results fed from HAMS was due to HAMS's separation in heave excitation force and radiation damping. However, no significant reflection is noted in the time domain results for NEMOH's separation in heave radiation damping. Thus, radiation damping variations are less reflected in the time domain simulations than the excitation force variations. The pitch mode motion results fed from HAMS exceeded the 5 % threshold. However, with a maximum rotation close to 6°, pitch RMSE remained at only 0.11°. Considering the motion range and environmental conditions, differences remained low for the preliminary design phase analysis.

Table 12 Time-domain analysis results of OC4-DeepCWind semi-submersible fed from compared panel method codes

		Rated wind speed case			50-year extreme case		
Value	Panel Method Code	Surge (m)	Heave (m)	Pitch (°)	Surge (m)	Heave (m)	Pitch (°)
Maximum	WAMIT	10.36	0.56	4.67	10.88	4.38	5.82
	NEMOH	10.35	0.56	4.66	10.84	4.39	5.82
	HAMS	10.35	0.52	4.64	10.92	4.08	5.67
	BEMUse	10.36	0.56	4.67	10.84	4.39	5.80
	CoV (%)	0.05	2.80	0.20	0.31	3.13	1.11
RMS	WAMIT	6.88	0.17	2.80	4.95	1.15	1.55
	NEMOH	6.88	0.16	2.80	4.94	1.15	1.54
	HAMS	6.88	0.15	2.80	4.95	1.08	1.52
	BEMUse	6.88	0.17	2.80	4.94	1.14	1.54
	CoV (%)	0.01	2.79	0.03	0.05	2.40	0.70
Mean	WAMIT	6.70	0.13	2.69	4.57	0.92	1.27
	NEMOH	6.70	0.13	2.69	4.57	0.92	1.26
	HAMS	6.70	0.12	2.69	4.57	0.87	1.25
	BEMUse	6.70	0.13	2.69	4.57	0.92	1.27
	CoV (%)	0.03	2.55	0.02	0.03	2.28	0.61
RMSE	WAMIT-ART	0.02	0.01	<0.1	0.01	0.06	<0.1
	NEMOH-ART	0.06	0.01	<0.1	0.02	0.07	<0.1
	HAMS-ART	0.01	0.03	<0.1	0.04	0.19	0.11
	BEMUse-ART	0.02	0.01	<0.1	0.02	0.08	<0.1
NRMSE (%)	WAMIT-ART	0.3	7.5	0.4	0.2	6.5	3.7
	NEMOH-ART	0.8	5.8	0.5	0.4	7.3	2.3
	HAMS-ART	0.2	19.7	0.8	0.9	20.5	9.0
	BEMUse-ART	0.4	8.6	0.4	0.5	8.8	4.1
NMAE (%)	WAMIT-ART	0.3	6.1	0.3	0.2	5.6	2.9
	NEMOH-ART	0.7	4.8	0.4	0.3	6.1	1.8
	HAMS-ART	0.2	16.0	0.6	0.7	17.4	7.1
	BEMUse-ART	0.3	7.0	0.3	0.4	7.4	3.2

6.3 Spectral density-based analyses

The spectral density-based analyses aimed to delineate the extent to which discrepancies in the frequency domain are reflected in time-domain calculations. For this purpose, PSD analyses, RAO analyses, and frequency range analyses were carried out. PSD analyses represented the power of floater motions regarding wave frequencies. Then, the floaters' responses to each wave frequency are analyzed with RAO. Finally, the agreement on the first-order wave excitation frequency range is questioned.

6.3.1 Power spectral density analyses

Figures 10 and 11 show the PSD values for OC3-Hywind and OC4-DeepCWind, respectively. Generally, differences for OC4-DeepCWind are more discernable than for OC3-Hywind. PSD values exhibit local peaks around the natural frequencies of each platform. Additionally, the local peaks are accompanied by increased deviations due to resonance, making the platform motion hard to identify.

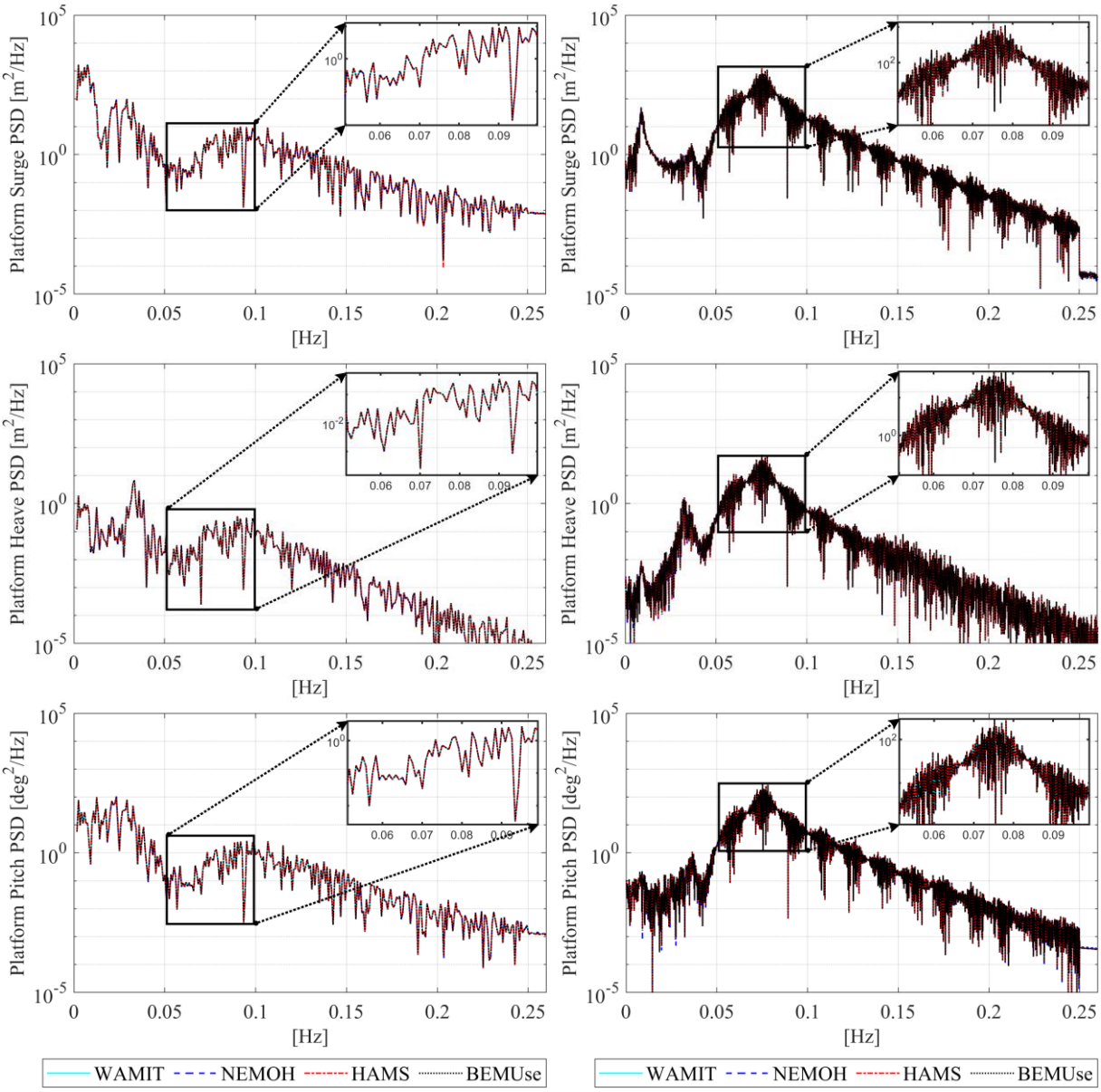

Fig. 10 OC3-Hywind PSD values for the rated wind speed case (left) and 50-year extreme case (right)

For all cases, the results of frequencies higher than 0.20 Hz have smaller powers than the lower part. Since smaller powers indicate smaller platform motions, discrepancies in frequencies higher than 0.20 Hz can be considered less significant.

OC3-Hywind Spar Buoy

In both environmental conditions, results almost overlapped, or the differences are not discernable except for a few points.

OC4-DeepCWind Semi-Submersible

For rated wind speed cases, observable discrepancies with high power ranged between 0.04 Hz and 0.08 Hz in heave mode. It was mostly around the natural frequency of 0.058 Hz, mainly due to HAMS. For pitch mode, differences were about 0.07 Hz, where HAMS makes some spikes.

For the 50-year extreme case, low PSD values at frequencies greater than 0.20 Hz for each mode showed disagreeing results as in the rated wind speed case. Discrepancies with high PSD values were observed below 0.05 Hz for the surge and pitch modes and between 0.02 Hz and 0.08 Hz for the heave mode.

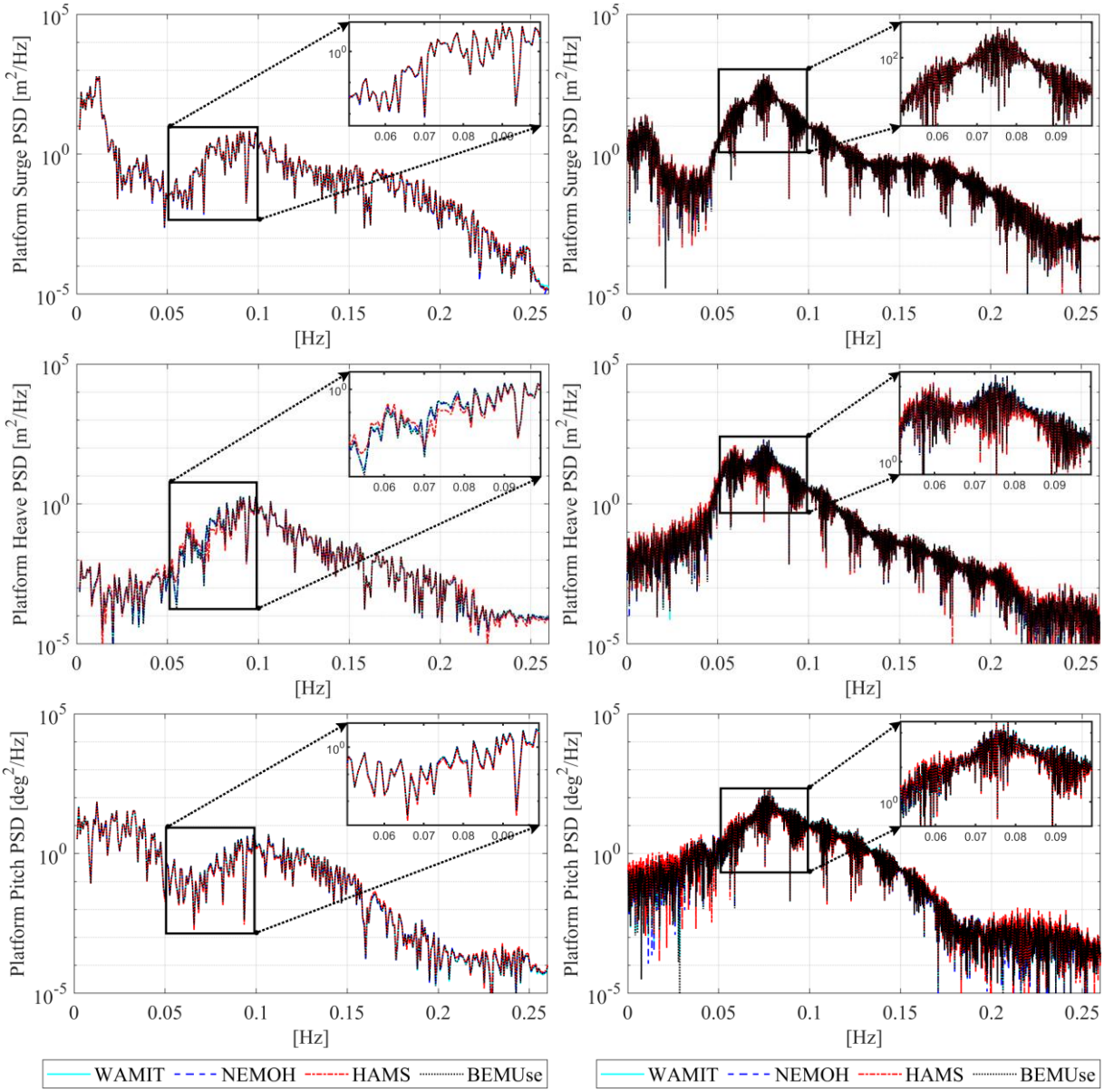

Fig. 11 OC4-DeepCWind PSD values for the rated wind speed case (left) and 50-year extreme case (right)

6.3.2 Response amplitude operator analyses

When CoV calculations were made for the PSD values, the CoV values approached infinity while the average PSD values remained below 0.001. Therefore, RAOs were chosen over PSDs to calculate the CoV. A-cut-off magnitude was set as 5 % for all RAO results to focus on a range where the environment affects the platform motion most. This method yielded zero CoV for regions with values below the 5 % RAO.

Figures 12 and 13 illustrate the RAO CoV values and the moving averages of RAO CoV for OC3-Hywind and OC4-DeepCWind, respectively. While ten values were averaged for the rated wind speed

cases, fifty values were averaged for the 50-year extreme case due to five times higher data density. The regions noted for PSD differences become more apparent with RAO CoV figures.

For both platforms, 50-year extreme conditions resulted in higher CoV rates than rated wind speed conditions. The higher CoV rates are attributed to the highly turbulent nature of the aerodynamics and hydrodynamics. Besides, the simulation time used for the extreme case is eight times longer than that of the rated wind speed case. Most notable discrepancies were below 0.05 Hz for both platforms, with greater prominence for 50-year extreme conditions.

For both environmental conditions, differences were minor for OC3-Hywind results than OC4-DeepCWind. The moving averaged deviations of OC3-Hywind did not exceed the 5 % threshold. Conversely, moving average deviations of OC4-DeepCWind exceeded the 5 % significance criterion threshold for many regions. The reasons are explained in subsection 6.2.2.

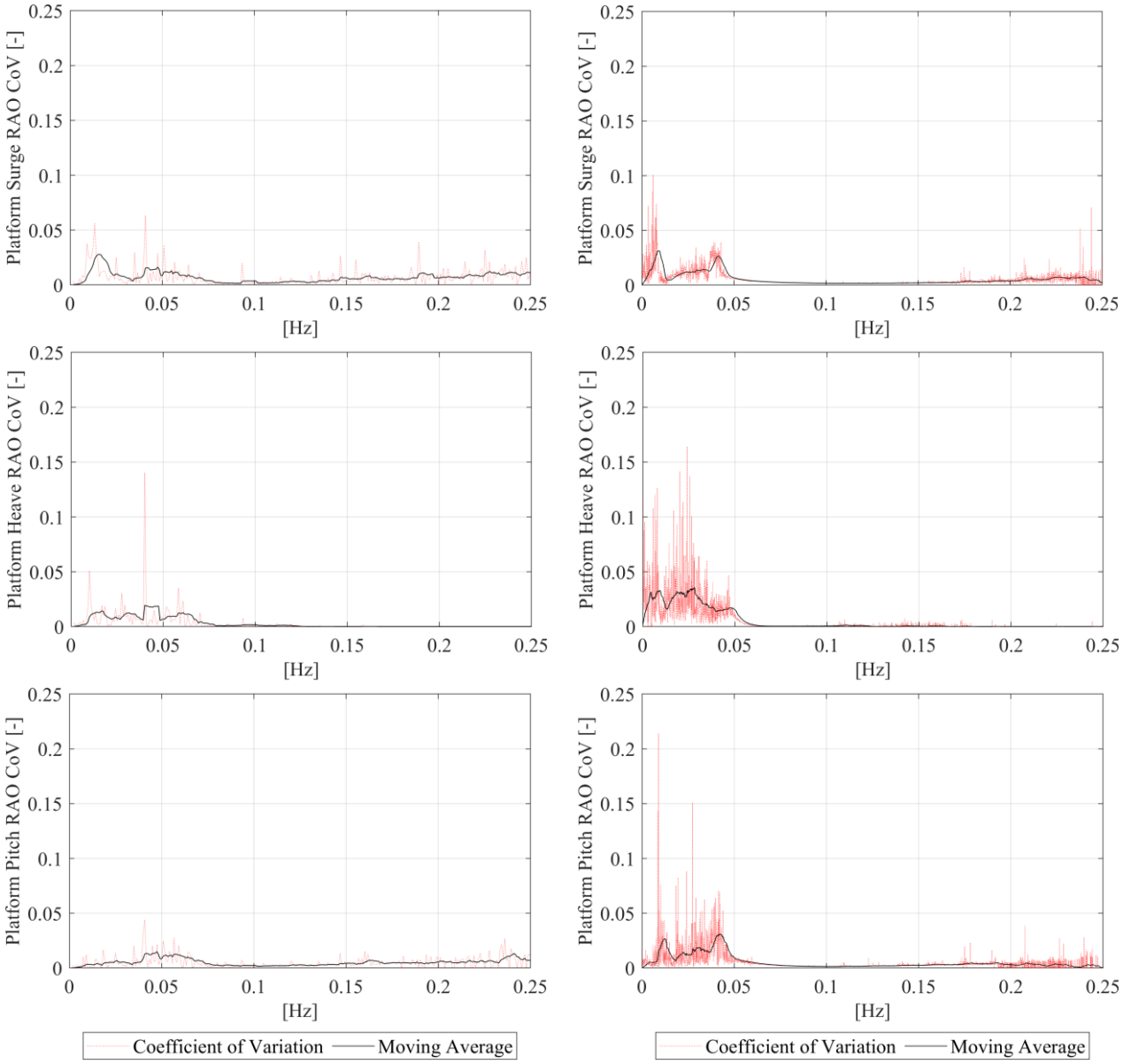

Fig. 12 OC3-Hywind RAO CoV values for the rated wind speed case (left) and 50-year extreme case (right)

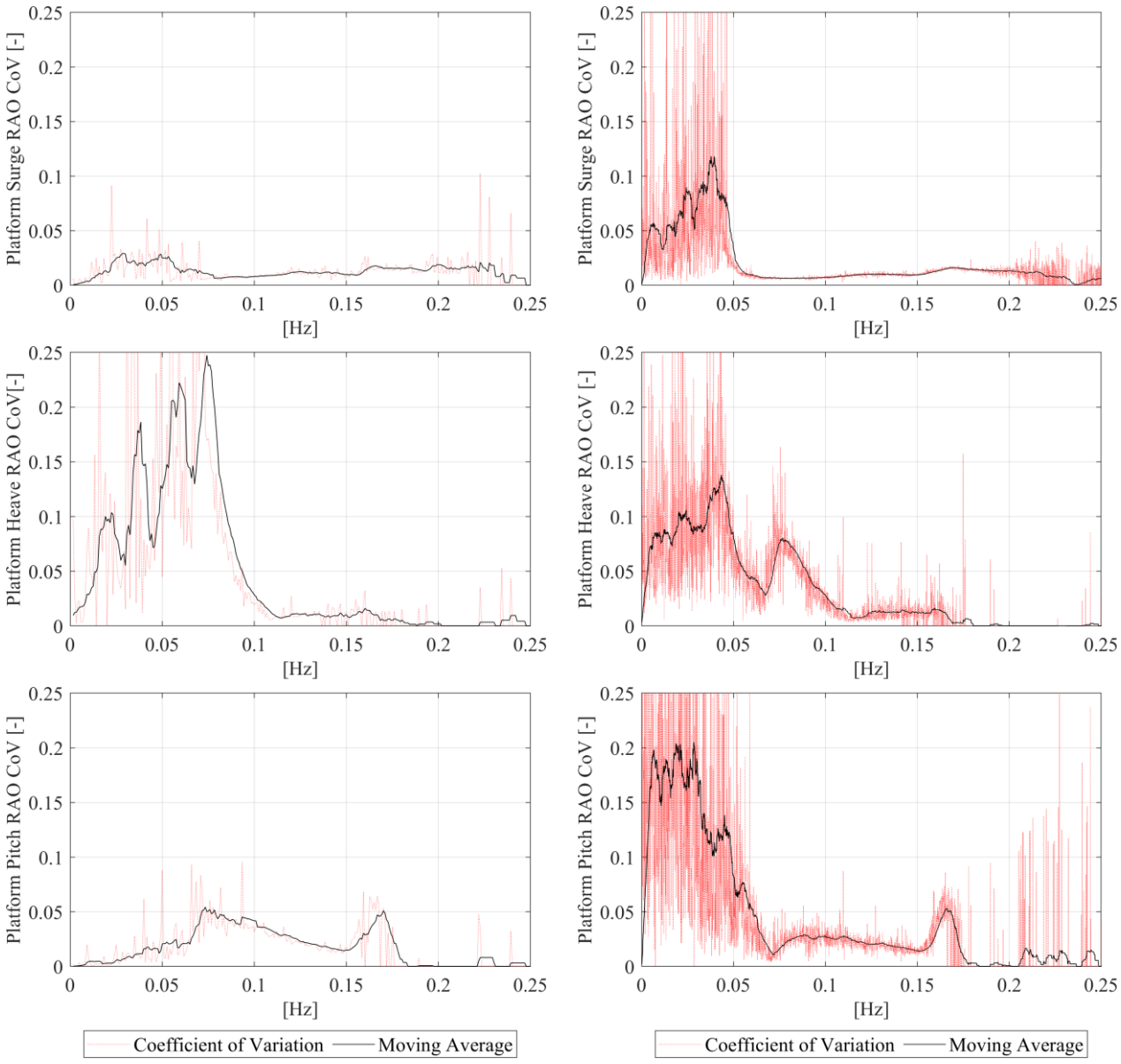

Fig. 13 OC4-DeepCWind RAO CoV values for the rated wind speed case (left) and 50-year extreme case (right)

6.3.3 Frequency-range analyses

Figures 12 and 13 highlight a notable zone of higher discrepancies at frequencies below 0.05 Hz. In contrast, as per DNV [49], the wave range from 0.04 Hz to 0.25 Hz carries significant wave energy. Separately evaluating the significant wave energy carrying range improves understanding of motion differences. Accordingly, ranges labeled as the “studied entire range” (0 Hz - 0.25 Hz) and the “first-order wave excitation range” (0.04 Hz - 0.25 Hz) were analyzed. The first-order wave excitation range focuses on frequencies affecting FWT platform motions the most.

For both platforms, filtering below 0.04 Hz significantly decreased the mean and the RMS of RAO CoV results. The highest decreases in the mean of RAO CoV belonged to the heave mode results. The only exception is the 50-year extreme case for OC4-DeepCWind, for which this was the pitch mode result. The highest decreases for RMS of RAO CoV were in the surge and heave modes.

Filtering results below 0.04 Hz showed mode-averaged decreases of around 50 % in mean and RMS RAO CoV for the 50-year extreme case, higher than those for the rated wind speed case. One reason is the increased RAO CoV in the pitch mode due to filtering. Nonetheless, the final pitch mode values remained below 2 % for mean RAO CoV and below 3 % for RMS RAO CoV, as shown in Table 13. Regarding the other reason, wave spectrum and inverse Fourier transformation cut-in and cut-off values of 0.04 Hz and 0.25

Hz were used for wave generation. However, generated waves below 0.04 Hz led to significant discrepancies. The longer simulation times of the 50-year extreme case might have led to more wave generation for frequencies lower than 0.04 Hz.

OC3-Hywind Spar Buoy

The mean and RMS of RAO CoV values for both environmental conditions were already less than 1.5 % before filtering results below 0.04 Hz. Nonetheless, the filtering led to significant decreases in the mean and RMS of RAO CoV, with a maximum of 76 %.

OC4-DeepCWind Semi-Submersible

Before filtering results of frequencies lower than 0.04 Hz, the mean values of RAO CoV were below the 5 % significance criterion. However, filtering led to a significant decrease in the mean RAO CoV values, which reduced below 2.5 % except for the heave mode result of the rated wind speed case.

Before filtering, the RMS of RAO CoV values exceeded the 5 % significance criterion for the heave mode results in both cases and the pitch mode in the 50-year extreme case. Except for the heave mode of the rated wind speed case, the filtering led to significant decreases and reduced the RMS of RAO CoVs below 5 %. Since only the heave natural frequency of OC4-DeepCWind was higher than 0.04 Hz, filtering below 0.04 Hz had a limited decrease in RAO CoV results for OC4-DeepCWind.

Consequently, the results fed from compared codes exhibit a higher agreement on the first-order wave excitation range, which is critical to platform performance. Comparing the RMS of RAO CoV values in Tables 7 and 13, discrepancies in the time domain simulation results stayed in the same order of magnitude as the discrepancies between panel method codes in FD analyses. The largest discrepancies were observed in heave mode and for OC4-DeepCWind.

Table 13 Mean and RMS of RAO CoV results for FAST outputs regarding WAMIT-NEMOH-HAMS-BEMUse inputs

		Rated wind speed case				50-year extreme case			
		OC3-Hywind		OC4-DeepCWind		OC3-Hywind		OC4-DeepCWind	
	Mode	Mean	RMS	Mean	RMS	Mean	RMS	Mean	RMS
Studied entire range (%)	Surge	0.73	1.10	1.30	1.79	0.54	0.90	2.11	4.85
	Heave	0.30	1.02	4.83	9.62	0.52	1.42	3.24	5.65
	Pitch	0.53	0.76	1.77	2.65	0.52	1.11	4.52	9.49
First-order wave excitation range (%)	Surge	0.66	0.98	1.25	1.70	0.37	0.54	1.19	2.12
	Heave	0.20	0.97	4.12	8.85	0.12	0.39	2.11	3.84
	Pitch	0.54	0.78	1.98	2.86	0.34	0.60	2.28	4.42
Difference (%)	Surge	10	12	4	5	31	40	43	56
	Heave	35	5	15	8	76	72	35	32
	Pitch	-3	-3	-12	-8	35	46	50	53

The time domain analysis began with free-decay analyses, examining hydro and mooring dynamics while excluding aero-servo-elasto dynamics. Then, time-domain platform motions were evaluated for both rated wind speed and 50-year extreme cases. The differences in platform motions remained within centimeters and below unit degrees. Despite longer simulation times and harsh environmental conditions in the 50-year extreme case, code results showed similar agreement levels with the rated wind speed case. Further investigation using PSDs and RAOs identified code differences in relevant wave frequencies. Local high PSD and RAO CoV values were attributed to resonance phenomena and observed discrepancies in panel method code outputs. Some frequency domain differences were less reflected in the time domain. For example, discrepancies in radiation damping were reflected less than those for excitation force. Finally, filtering narrowed the focus to the first-order wave excitation range, highlighting improved agreement between panel method codes. The analyses provide insights into the impact of panel method codes on platform motions as a reflection of frequency domain results.

7. Conclusion

This study investigated the impact of hydrodynamic calculations from various panel method codes on the time-domain responses of floating wind turbines. Three open-source panel method codes (NEMOH, HAMS, BEMUse) and WAMIT were compared. These panel method codes deliver hydrodynamic data in the frequency domain. The outputs are then used for time-domain simulations of OC3-Hywind spar buoy and OC4-DeepCWind semi-submersible platforms. Evaluation metrics consisting of normalized mean absolute error, normalized root mean squared error, and coefficient of variation were used to assess differences with a 5 % significance criterion threshold. Analyses focused on surge, heave, and pitch modes as the modes incited by head waves.

Regarding the mesh refinement study, HAMS and BEMUse were the most efficient in computational time. The most and the least mesh-sensitive results were heave radiation damping, and surge added mass, respectively. The convergence behavior of the panel method codes changed with platforms.

The frequency-domain analysis revealed close agreement for OC3-Hywind. For OC4-DeepCWind, there was a good agreement with some exceptions in the heave mode, which is attributed to the lower mesh convergence rates of the semi-submersible. NMAE values of less than 1 % are recommended in mesh convergence analysis for better agreement among panel method codes.

Time-domain analysis under operational and extreme conditions indicated close agreement among panel method codes. The deviations in resultant motion outputs remained within a few centimeters and below unit degrees. Spectral density-based analyses showed higher agreement within the 0.04 Hz - 0.25 Hz (i.e., first-order wave excitation range). Discrepancies at lower frequencies were attributed to resonance, making the platform motion hard to identify.

Overall, it is shown that the reflections of panel method code outputs on time-domain responses changed with the platforms and modes. However, differences in the resultant motions remained within centimeters and below unit degrees, even under extreme environmental conditions and for longer simulation times. Also, the spectral density-based analyses indicated a high agreement. Therefore, using WAMIT or open-source codes, NEMOH, HAMS, and BEMUse, can yield nearly identical outputs for time-domain estimations of floating wind turbines.

REFERENCES

[1] WindEurope, 2017. Floating Offshore Wind Vision Statement. https://windeurope.org/wp-content/uploads/files/about-wind/reports/Floating-offshore-statement.pdf. accessed 5th December 2024.

[2] Uzunoglu, E., Guedes Soares, C., 2019. A system for the hydrodynamic design of tension leg platforms of floating wind turbines. *Ocean Engineering*, 171, 78–92. https://doi.org/10.1016/j.oceaneng.2018.10.052

[3] Zhang, Y., Xu, H., Law, Y., Santo, H., Magee, A., 2023. Hydrodynamic analysis and validation of the floating DeepCwind semi-submersible under 3-h irregular wave with the HOS and CFD coupling method. *Ocean Engineering*, 287, 115701. https://doi.org/10.1016/j.oceaneng.2023.115701

[4] Zhang, W., Calderon-Sanchez, J., Duque, D., Souto-Iglesias, A., 2024. Computational Fluid Dynamics (CFD) applications in Floating Offshore Wind Turbine (FOWT) dynamics: A review. *Applied Ocean Research*, 150, 104075. https://doi.org/10.1016/j.apor.2024.104075

[5] Uzunoglu, E., Guedes Soares, C., 2018. On the model uncertainty of wave induced platform motions and mooring loads of a semisubmersible based wind turbine. *Ocean Engineering*, 148, 277–285. https://doi.org/10.1016/j.oceaneng.2017.11.001

[6] Sclavounos, P., Tracy, C., Lee, S., 2008. Floating Offshore Wind Turbines: Responses in a Seastate Pareto Optimal Designs and Economic Assessment. *Volume 6: Nick Newman Symposium on Marine Hydrodynamics; Yoshida and Maeda Special Symposium on Ocean Space Utilization; Special Symposium on Offshore Renewable Energy*, ASME. https://doi.org/10.1115/OMAE2008-57056

[7] Lee, J. Y., Lim, S. J., 2008. Hull form optimization of a tension-leg platform based on coupled analysis. *18th International Offshore Polar Engineering Conference*, 6-11 July, Vancouver, Canada, 100–107.

[8] Uzunoglu, E., Guedes Soares, C., 2018. Parametric modelling of marine structures for hydrodynamic calculations. *Ocean Engineering*, 160, 181–196. https://doi.org/10.1016/j.oceaneng.2018.04.049

[9] Wayman, E. N., Sclavounos, P. D., Butterfield, S., Jonkman, J., Musial, W., 2006. Coupled Dynamic Modeling of Floating Wind Turbine Systems. *Offshore Technology Conference*, 1-4 May, Houston, Texas, USA. https://doi.org/10.4043/18287-MS

[10] Coulling, A. J., Goupee, A. J., Robertson, A. N., Jonkman, J. M., Dagher, H. J., 2013. Validation of a FAST semi-submersible floating wind turbine numerical model with DeepCwind test data. *Journal of Renewable and Sustainable Energy*, 5(2), 023116. https://doi.org/10.1063/1.4796197

[11] Oguz, E., Clelland, D., Day, A. H., Incecik, A., López, J. A., Sánchez, G., Almeria, G. G., 2018. Experimental and numerical analysis of a TLP floating offshore wind turbine. *Ocean Engineering*, 147, 591–605. https://doi.org/10.1016/j.oceaneng.2017.10.052

[12] Babarit, A., Delhommeau, G., 2015. Theoretical and numerical aspects of the open source BEM solver NEMOH. *11th European Wave and Tidal Energy Conference*, 6-11 September, Nantes, France.

[13] Kurnia, R., Ducrozet, G., Gilloteaux, J.-C., 2022. Second Order Difference- and Sum-Frequency Wave Loads in the Open-Source Potential Flow Solver NEMOH. *41st International Conference on Ocean, Offshore and Arctic Engineering*, 5-10 June, Hamburg, Germany. https://doi.org/10.1115/OMAE2022-79163

[14] Liu, Y., 2019. HAMS: A Frequency-Domain Preprocessor for Wave-Structure Interactions—Theory, Development, and Application. *Journal of Marine Science and Engineering*, 7(3), 81. https://doi.org/10.3390/jmse7030081

[15] Liu, Y., 2021. Introduction of the Open-Source Boundary Element Method Solver HAMS to the Ocean Renewable Energy Community. *14th European Wave and Tidal Energy Conference*, 5-9 September, Plymouth, United Kingdom.

[16] Saverin, J. R., Grüter, L., 2022. Quadrature Schemes for the Integration of the Free-Surface Green's Function Within the Open-Source Boundary Element Method Library BEMUse. *Volume 7: CFD and FSI*, American Society of Mechanical Engineers. https://doi.org/10.1115/OMAE2022-80831

[17] Uzunoglu, E., Liu, Y., Guedes Soares, C., 2022. Performance of the open-source potential flow solver HAMS in estimating the hydrodynamic properties of a floating wind turbine. *Trends in Renewable Energies Offshore*, London: CRC Press, 619-627. https://doi.org/10.1201/9781003360773-70

[18] Ucar, M., Uzunoglu, E., Oguz, E., 2022. Comparison and Evaluation of Open-Source Panel Method Codes against Commercial Codes. *GMO Journal of Ship and Marine Technology*, 221, 86-108. https://doi.org/10.54926/gdt.1106386

[19] Ancellin, M., Nguyen, N., 2024. Case Studies of BEM Solver Accuracy With the Open-Source Code Capytaine. *Volume 7: Ocean Renewable Energy*, ASME. https://doi.org/10.1115/OMAE2024-127995

[20] Penalba, M., Kelly, T., Ringwood, J., 2017. Using NEMOH for Modelling Wave Energy Converters: A Comparative Study with WAMIT. *12th European Wave and Tidal Energy Conference*, 27 August – 1 September, Cork, United Kingdom.

[21] Bhinder, M. A., Murphy, J., 2019. Evaluation of the Viscous Drag for a Domed Cylindrical Moored Wave Energy Converter. *Journal of Marine Science and Engineering*, 7(4), 120. https://doi.org/10.3390/jmse7040120

[22] Raghavan, V., Lavidas, G., Metrikine, A. V., Mantadakis, N., Loukogeorgaki, E., 2022. A comparative study on BEM solvers for Wave Energy Converters. *Trends in Renewable Energies Offshore*, London: CRC Press, 441-447. https://doi.org/10.1201/9781003360773-50

[23] Ancellin, M., Dias, F., 2019. Capytaine: a Python-based linear potential flow solver. *Journal of Open Source Software*, 36(4), 1341. https://doi.org/10.21105/joss.01341

[24] Kurnia, R., Ducrozet, G., 2023. NEMOH: Open-source boundary element solver for computation of first- and second-order hydrodynamic loads in the frequency domain. *Computer Physics Communications*, 292, 108885. https://doi.org/10.1016/j.cpc.2023.108885

[25] Liang, L., Baoji, Z., Hao, Z., Hailin, T., Weijie, W., 2023. Hydrodynamic performance optimization of marine propellers based on fluid-structure coupling. *Brodogradnja*, 74(3), 145-164. https://doi.org/10.21278/brod74308

[26] Bal K., Bural, D. B., 2024. Investigation into forces on offshore piles with constant and linearly varying diameters using CFD and extended Morison equation under separate wave and current loadings. *Brodogradnja*, 75(4), 1-19. https://doi.org/10.21278/brod75406

[27] Zhang, Y., Li, D., Hong, S., Zhang, M., 2023. Design of a new oscillating-buoy type wave energy converter and numerical study on its hydrodynamic performance. *Brodogradnja*, 74(1), 145-168. https://doi.org/10.21278/brod74108

[28] Hadi, E. S., Tuswan, T., Azizah, G., Ali, B., Samuel, S., Hakim, M. L., Hadi, M. R. C. P., Iqbal, M., Sari, D. P., Satrio, D., 2023. Influence of the canal width and depth on the resistance of 750 DWT Perintis ship using CFD simulation. *Brodogradnja*, 74(1), 117-144. https://doi.org/10.21278/brod74107

[29] Yin, Z.-Y., 2022. Three-dimensional numerical modelling of progressive failure of caisson foundation in sand using a coupled FDM–DEM method. *Ocean Engineering*, 253, 111332. https://doi.org/10.1016/j.oceaneng.2022.111332

[30] Lee, C. H., Newman, J. N., 2006. WAMIT USER MANUAL, Chestnut Hill, MA. https://www.wamit.com/manualupdate/v74_manual.pdf (Accessed Dec. 5, 2024).

[31] Newman J.N, 1977. Marine Hydrodynamics. *MIT press*, London, UK. https://doi.org/10.7551/mitpress/4443.001.0001

[32] Newman, J. N., 1985. Algorithms for the free-surface Green function. *Journal of Engineering Mathematics*, 19(1), 57-67. https://doi.org/10.1007/BF00055041

[33] Newman, J. N., 1992. The approximation of free-surface Green functions. *Wave Asymptotics*, P. A. Martin and G. R. Wickham, Eds., Cambridge: Cambridge University Press, 107-135.

[34] Liu, Y., Iwashita, H., Hu, C., 2015. A calculation method for finite depth free-surface green function. *International Journal of Naval Architecture and Ocean Engineering*, 7(2), 375-389. https://doi.org/10.1515/ijnaoe-2015-0026

[35] Liu, Y., Yoshida, S., Hu, C., Sueyoshi, M., Sun, L., Gao, J., Cong, P., He., G, 2018. A reliable open-source package for performance evaluation of floating renewable energy systems in coastal and offshore regions. *Energy Conversion and Management*, 174, 516-536. https://doi.org/10.1016/j.enconman.2018.08.012

[36] Sheng, W., Tapoglu, E., Ma, X., Taylon, C. J., Dorell, R. M., Parsons, D. R., Aggidis, G., 2022. Hydrodynamic studies of floating structures: Comparison of wave-structure interaction modelling. *Ocean Engineering*, 249, 110878. https://doi.org/10.1016/j.oceaneng.2022.110878

[37] Liu, Y., 2024. An open-source computer program for the analysis of wave diffraction and radiation of three-dimensional floating or submerged structures. https://github.com/YingyiLiu/HAMS (Accessed Dec. 5, 2024).

[38] Raghavan, V., Loukogeorgaki, E., Mantadakis, N., Metrikine, A.V., Lavidas, G., 2024. HAMS-MREL, a new open source multiple body solver for marine renewable energies: Model description, application and validation. *Renewable Energy*, 237, 121577. https://doi.org/10.1016/j.renene.2024.121577

[39] Jonkman, J. M., 2007. Dynamics Modeling and Loads Analysis of an Offshore Floating Wind Turbine, Golden, CO. https://doi.org/10.2172/921803

[40] Jonkman, J. M., Buhl, M. L., 2005. FAST User's Guide. Golden, Colorado. https://www.nrel.gov/docs/fy06osti/38230.pdf. accessed 5th December 2024.

[41] Jonkman, J. M., Robertson, A. N., Hayman, G. J., 2014. HydroDyn User's Guide and Theory Manual. https://www.nrel.gov/wind/nwtc/assets/downloads/HydroDyn/HydroDyn_Manual.pdf. accessed 5th December 2024.

[42] Zabala, I., Pena-Sanchez, Y., Kelly, T., Henriques, J. C. C., Penalba, M., Faedo, N., Ringwood, J. V., Blancov, J. M., 2021. BEMRosetta: An open-source hydrodynamic coefficients converter and viewer integrated with Nemoh and FOAMM. *14th European Wave and Tidal Energy Conference*, 5-9 September, Plymouth, United Kingdom.

[43] Hmedi, M., Uzunoglu, E., Guedes Soares, C., 2022. Influence of platform configuration on the hydrodynamic performance of semi-submersibles for offshore wind energy. *Trends in Maritime Technology and Engineering Volume 2*, London: CRC Press, 411-420. https://doi.org/10.1201/9781003320289-43

[44] Statoil, 2015. Hywind Scotland Pilot Park: Environmental Statement. https://tethys.pnnl.gov/sites/default/files/publications/Hywind-Pilot-Park-Environmental-Statement.pdf. accessed 5th December 2024.

[45] Helder, J. A., Pietersma, M., 2013. UMaine – DeepCwind/OC4 Semi Floating Wind Turbine Repeat Tests, Wageningen, The Netherlands.

[46] Jonkman, J., Musial, W., 2010. Offshore Code Comparison Collaboration (OC3) for IEA Wind Task 23 Offshore Wind Technology and Deployment. https://doi.org/10.2172/1004009

[47] Robertson, A., Jonkman, J., Masciola, M., Song, H., Goupee, A., Coulling, A., Luan, C., 2014. Definition of the Semisubmersible Floating System for Phase II of OC4. https://doi.org/10.2172/1155123

[48] Robertson, A., Jonkman, J., Vorpahl, F., Popko, W., Qvist, J., Frøyd, L., Chen, X., Azcona, J., Uzunoglu, E., Guedes Soares, C., Luan, C., Yutong, H., Pengcheng, F., Yde, A., Larsen, T., Nichols, J., Buils, R., Lei, L., Nygaard, T. A., Manolas, D., Heege, A., Vatne, S. R., Ormberg, H., Duarte, T., Godreau, C., Hansen, H. F., Nielsen, A. W., Riber, H., Le Cunff, C., Beyer, F., Yamaguchi, A., Jung, K. J., Shin, H., Shi, W., Park, W., Alves, M., Guérinel, M., 2014. Offshore Code Comparison Collaboration Continuation Within IEA Wind Task 30: Phase II Results Regarding a Floating Semisubmersible Wind System. *Volume 9B: Ocean Renewable Energy*, American Society of Mechanical Engineers. https://doi.org/10.1115/OMAE2014-24040

[49] DNV GL, 2018. DNVGL-ST-0119: Floating Wind Turbine Structures.

[50] Li, L., Gao, Z.., Moan, T., 2013. Joint Environmental Data at Five European Offshore Sites for Design of Combined Wind and Wave Energy Devices. *Volume 8: Ocean Renewable Energy*, American Society of Mechanical Engineers. https://doi.org/10.1115/OMAE2013-10156

[51] Jonkman, B. J., 2009. TurbSim User's Guide: Version 1.50, United States. https://doi.org/10.2172/965520

[52] IEC, 2019. Wind Turbines – Part 3: Design Requirements for Offshore Wind Turbines. *IEC 61400-3, 1st ed.*, Geneva, Switzerland.

[53] NREL, 2015. Hydrodynamic analysis of OC3-Hywind spar buoy. https://forums.nrel.gov/t/hydrodynamic-analysis-of-oc3-hywind-spar-buoy/1103. accessed 5th December 2024.

[54] DNV, 2004. Recommended Practice DNV-RP-F205, Global performance analysis of deepwater floating structures.

[55] Uzunoglu, E., Guedes Soares, G., 2015. Influence of bracings on the hydrodynamic modelling of a semi-submersible offshore wind turbine platform. *Renewable Energies Offshore*, 755-762. https://doi.org/10.1201/b18973-106

[56] Ko, K. H., Park, T., Kim, K. H., Kim, Y. Yoon, D. H., 2011. Development of panel generation system for seakeeping analysis. *CAD Computer Aided Design*, 43(8), 848-862. https://doi.org/10.1016/j.cad.2011.04.013

[57] Jafaryeganeh, H., Rodrigues, J. M., Guedes Soares, C., 2014. Influence of mesh refinement on the motions predicted by a panel code. *Maritime Technology and Engineering*, C. Guedes Soares, Ed., London: Taylor & Francis Group.

[58] Uzunoglu, E., Guedes Soares, C., 2020. Hydrodynamic design of a free-float capable tension leg platform for a 10 MW wind turbine. *Ocean Engineering*, 197. https://doi.org/10.1016/j.oceaneng.2019.106888

[59] Uzunoglu, E., Guedes Soares, C., 2015. Comparison of numerical and experimental data for a DeepCwind type semi-submersible floating offshore wind turbine. *Renewable Energies Offshore* -, 24-26 November, Lisbon, Portugal, 747-754. https://doi.org/10.1201/b18973-105